



Numerical analysis of the effect of porous structure on free convection heat transfer inside an eccentric annular space

Gazy F. Al-Sumaily ^{a,c,*}, Hasanen M. Hussen ^b, Miqdam T. Chaichan ^a, Hayder A. Dhahad ^b,
Mark C. Thompson ^c

^a Energy and Renewable Energies Technology Centre, University of Technology, Iraq

^b Mechanical Engineering Department, University of Technology, Iraq

^c Department of Mechanical and Aerospace Engineering, Monash University, Australia



ARTICLE INFO

Keywords:

Free convection
Eccentric annular enclosure
Laminar flow
Porous media
Packed bed
Local thermal non-equilibrium

ABSTRACT

In the literature, there are some conclusions seem to be conflicting about the effect of porous structure of a packed bed of spheres, in particular the effects of the sphere diameter and the porosity on the heat transfer by convection. For this reason, the present numerical analysis investigates the effects of these two parameters on natural convection heat transfer inside an eccentric annulus packed with stationary spheres. More reliable models for energy and momentum transport in porous media, namely the two-phase energy model that fails to postulate local thermal equilibrium "LTE" status between the solid spheres and the flowing fluid, and the full Darcy–Brinkman–Forchheimer momentum model, are employed. This non-dimensional analysis is conducted for different spheres' sizes (annulus interior cylinder/sphere diameter ratio, $D_i/d = 20 - 100$), porosities ($\epsilon = 0.3 - 0.7$), and sphere materials (solid/fluid thermal conductivity ratio, $K_r = 1 - 10^5$), and at various heating represented by Rayleigh number ($Ra = 8 \times 10^7 - 2 \times 10^8$). The results show that the effects of these parameters depends strongly on the thermal conductivity of the spheres material. Thus, it was found that at lower thermal conductivity ratio, the bigger sphere size or the larger porosity produces the higher convection heat transfer. However, at moderate thermal conductivity ratio, the convection heat transfer can be increased or decreased as the sphere size or the porosity increases. But, at higher thermal conductivity ratio, the increase in the sphere size or the porosity causes a decrease in the convection heat transfer.

1. Introduction

In the thermal engineering applications, porous media may be employed as an insulator or an effectual technique for heat transfer enhancement depending on their thermal conductivity. Indeed, in these thermal applications, porous media can be used as a fibrous material or a packed bed of spheres. In packed beds, it is essential to characterise the fluid flow within it as a function of sphere diameter and porosity. Achenbach [1] published a thorough review on flow and thermal characteristics in packed beds. It has come to our attention from the literature that there are number of evidently conflicting findings regarding of the reliance of convection heat transfer on the porous structure, especially, the sphere diameter and the porosity. For example, David and Cheng [2], Kwendakwema and Boehm [3], Hsiao et al. [4], Wang and Du [5], and Jiang et al. [6], found that the increase in the sphere diameter causes an increase in the rate of

heat transfer. Kwendakwema and Boehm [3] examined numerically mixed convective flow in an annular space between two concentric vertical cylinders filled with a fibrous material. The outer cylinder was considered to be at constant temperature, while the inner cylinder was assumed insulated. They employed Darcy model to predict the fluid flow, while the local thermal equilibrium energy formulation was employed to calculate the temperature field. Wang and Du [5] performed an experimental study to investigate forced convection heat transfer in a water-glass porous medium inside a vertical annulus.

The opposite behaviour has been obtained by Jeigarnik et al. [7], Hwang and Chao [8], Nasr et al. [9], Chen and Hadim [10], Jiang et al. [11], Saito and Lemos [12], and Blaszcuk et al. [13]. This contradiction is attributed to be due to the discrepancy between the thermal conductivities of both fluid and solid phases, as clarified priorly by Jiang et al. [6]. They mentioned that when the solid/fluid

* Corresponding author at: Energy and Renewable Energies Technology Centre, University of Technology, Iraq.

E-mail addresses: gazy.alsumaily@monash.edu (G.F. Al-Sumaily), hasanen.m.hussen@uotechnology.edu.iq (H.M. Hussen), miqdam.t.chaichan@uotechnology.edu.iq (M.T. Chaichan), hayder.a.dhahad@uotechnology.edu.iq (H.A. Dhahad), mark.thompson@monash.edu (M.C. Thompson).

thermal conductivity ratio is greater than unity, the convective heat transfer coefficient close to the hot wall is primarily controlled by direct conduction within solid spheres. Consequently, this coefficient decreases as the sphere diameter increases as a consequence of the reduction in the contact surface between the hot wall and the solid spheres. On the other hand, when the solid/fluid thermal conductivity ratio is almost unity, the heat transfer from the surface is mainly governed by convection, and therefore when the sphere size enlarges, this leads to an increase in the thermal dispersion, and consequently the heat transfer by convection become stronger.

In addition, a non-linear influence of the sphere size on the convection heat transfer has been found by Jiang et al. [14], Jiang et al. [15], Al-Sumaily et al. [16]. They concluded that the increase in the sphere size can lead to a decrease or an increase in convection heat transfer depending on other parameters such as solid and fluid thermal conductivities, thermal dispersion, mass flow rate, and porosity. Jiang et al. [14] conducted numerical simulations for modelling forced convection flow within a horizontal channel heated from above by iso-flux and packed with metallic spheres. Jiang et al. [15] tested experimentally similar physical case, but for different kinds of spheres, i.e., stainless steel, glass, and bronze, saturated by water, were utilised in their investigation. The experimental results indicated that the increase in the sphere size increases the surface heat transfer for the channel with glass spheres. However, an adverse trend of results was observed when filling the channel with bronze or stainless steel, at various mass flow rates. Al-Sumaily et al. [16] studied the influence of particle size of spheres inside a horizontal packed bed containing a hot cylinder under forced convection. The results showed that the convection heat transfer from the cylinder can be increased or decreased as the particle size enlarges, relying on many other related variables like thermal dispersion, solid/fluid thermal conductivity ratio, Reynolds number, and the interphase convective coefficient.

Regarding the porosity, in the works of Jue [17], Pavel [18], Layeghi and Nouri-Borujerdi [19], Huang et al. [20], Mabrouk et al. [21], and Lu et al. [22], they revealed that employing lower-porosity porous media enhances the convective heat transfer. For instance, Jue [17] studied free convection inside a porous cavity having an internal heat generation. The objective of his work was to study the influence of existence of the porous material on the hydrodynamic and thermal characteristics generated by sidewall heating in addition to the interior heat source. The results showed that a higher porosity value produces a smaller Nusselt number value. Pavel [18] who conducted numerical and experimental studies to investigate the impact of inserting a metallic porous material inside a pipe on the heat transfer rates. It was concluded that higher rates of heat could be obtained by raising Reynolds number and/or by decreasing the porosity. Layeghi and Nouri-Borujerdi [19] examined forced convection heat transfer from a circular cylinder using the Darcy model for a small range of Péclet number ($\text{Pe} \leq 40$). They examined the influence of permeability and porosity on the temperature distribution and the convective heat transfer from the cylinder. Huang et al. [20] studied the augmentation of heat transfer by inserting a porous substrate inside a tube, for both laminar and turbulent flows. They found that inserting a porous medium can enhance the heat transfer considerably. However, they also found that the higher enhancement can be obtained at lower porosity in both laminar and turbulent regimes. Mabrouk et al. [21] studied numerically the effect of porosity on unsteady forced convective flow within an open-ended horizontal channel stuffed with phase change material (PCM) and porous structure. They found that using lower porosity materials inside a high strength flow enhances the thermal convection performance in the channel. Lu et al. [22] investigated experimentally the effects of porosity and pore diameter on free convection within an open cell copper foam. Their results showed that the porosity does not have a significant impact on the heat transfer performance when it is less than 78%; however, as it increases beyond this value, the convection heat transfer starts decreasing considerably.

On the other hand, the numerical works of Saito and Lemos [12] and Wong and Saeid [23] showed opposite trend of results. Thus, Saito and Lemos [12] who investigated forced convection inside a horizontal porous plate channel, reported that when the higher porosity is used, the higher the Nusselt number is acquired. They justified this finding as higher porosity produces lower interfacial area, which decreases the energy exchange between the fluid and solid phases, then causing higher Nusselt numbers. Wong and Saeid [23] who also used the thermal non-equilibrium energy model to study mixed convection of jet impingement cooling of a heat source placed inside a porous channel, found that Nusselt number can be augmented by increasing the porosity value.

In order to participate and provide another opinion in the literature about the effects of particle diameter and porosity on convection heat transfer, the current study was conducted to study free convection inside a packed bed of spheres within an annular space between two eccentric horizontal circular cylinders. Firstly, this physical problem was chosen because it has a feasible importance in numerous thermal engineering applications such as cooling of high-energy electronic devices, solar collectors, cooling of nuclear reactor core, and thermal storage systems, as well as the devices that include thermal insulators. Also, indeed, buoyancy-driven flows inside eccentric annular porous spaces are intricate to be solved numerically; therefore, the attempts to study such case are infrequent. Secondly, in this study, a more reliable momentum model that includes non-Darcian effects such as the effects of inertia and thermal dispersion, is incorporated along with the *Local Thermal non-Equilibrium* “LTNE”- energy model, to precisely calculate the velocity and temperature fields during the annular packed bed. As a result, the aim is to analyse and quantify correctly and accurately the influences of particle diameter and porosity on free convection as well as the heat conduction, taking all the non-Darcian effects into consideration and without the assumption of thermal equilibrium between the solid and fluid phases.

2. Problem description

The physical problem under study along with the selected coordinate system are demonstrated in Fig. 1. As displayed, a circular cylinder having a diameter of (D_i) and a wall temperature of (T_h) is submerged eccentrically in an encompassed round packed bed of spherical particles saturated with air and having a diameter of (D_o) and a wall temperature of (T_c), where ($D_o = 3D_i$). The spherical particles of the packed bed, which are considered to have a particle diameter of (d), are assumed to be stationary in the annular space, and air is moving throughout them by the action of buoyancy-driven forces. The centre of the internal hot cylinder is shifted upward from the centre of the external cold cylinder by an eccentric length of ($e = 0.8$). The inner and outer cylinders' surfaces are assumed to be impermeable. The physical case is considered that at time ($t > 0$), the inner cylinder wall is abruptly heated to (T_h), and thereafter kept at this hot temperature. Indeed, this unexpected alteration in the temperature could establish prospective unsteadiness in the flow and thermal systems for ($T_h > T_c$), thus, triggering buoyancy driven steady or unsteady free convective airflows in the annular gap.

3. Mathematical formulations

It is assumed that the convective fluid flow is incompressible and viscous, and is characterised by the *Brinkman-Forchheimer-extended Darcy* model. Also, it is presumed that the gravitation acts downwards, and the properties of the fluid phase are kept constant, except for the density, which changes with the temperature according to the Boussinesq approximation. Additionally, the following presumptions are also implemented: The packed bed is isotropic and homogeneous; no interior heat generation takes place inside the packed bed; the interfacial radiation heat transfer between the phases of the bed is

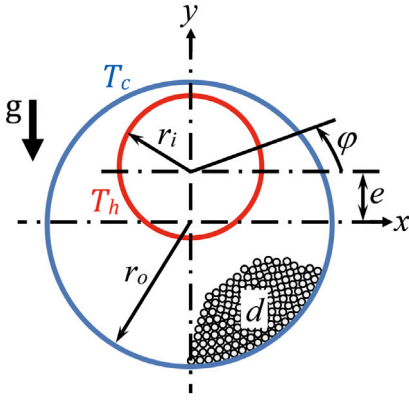


Fig. 1. Configuration of the eccentric annular packed bed of spheres with system coordinates.

neglected; and the packed bed is saturated with air, so Prandtl number is considered as ($\text{Pr} = 0.71$). But, substantially, the solid particles and air are in *Local Thermal non-Equilibrium "LTNE"* condition all over the bed. Accordingly, the mass, momentum and energy equations could be scripted in the following dimensional formulas described in (Vafai and Sozen [24], Amiri and Vafai [25], Al-Sumaily et al. [26]):

$$\frac{\partial u}{\partial x} + \frac{\partial v}{\partial y} = 0, \quad (1)$$

$$\frac{\rho_f}{\epsilon^2} \left(u \frac{\partial u}{\partial x} + v \frac{\partial u}{\partial y} \right) = -\frac{\mu_f}{K} u - \frac{\rho_f C_F}{\sqrt{K}} |\bar{u}| u + \frac{\mu_f}{\epsilon} (\nabla^2 u) - \frac{\partial p_f}{\partial x}, \quad (2)$$

$$\frac{\rho_f}{\epsilon^2} \left(u \frac{\partial v}{\partial x} + v \frac{\partial v}{\partial y} \right) = -\frac{\mu_f}{K} v - \frac{\rho_f C_F}{\sqrt{K}} |\bar{u}| v + \frac{\mu_f}{\epsilon} (\nabla^2 v) - \frac{\partial p_f}{\partial y} + \rho_f g \beta (T_f - T_c), \quad (3)$$

$$\epsilon (\rho c_p)_f \left(u \frac{\partial T_f}{\partial x} + v \frac{\partial T_f}{\partial y} \right) = k_{f,\text{eff},(x,y)} (\nabla^2 T_f) + h_{sf} a_{sf} (T_s - T_f), \quad (4)$$

$$\kappa_{s,\text{eff}} (\nabla^2 T_s) - h_{sf} a_{sf} (T_s - T_f) = 0, \quad (5)$$

where (u) and (v) represent the dimensional horizontal and vertical velocities, respectively, (x) and (y) represent the dimensional system coordinates, (T) is the dimensional temperature, and (p_f) is the dimensional pressure. Also, (c_p) is the heat capacity, (μ_f) is the dynamic viscosity, and (ρ) is the density. For the packed bed, (a_{sf}) is the

interfacial specific surface area, (C_F) is the inertia coefficient, (h_{sf}) is the particle-to-air convective coefficient, (K) is the permeability, and ((ϵ)) is the porosity. Whereas, the subscripts (s) and (f) indicate to the solid and fluid phases, respectively, while (eff) refers to the effective quality, thereby, ($k_{f,\text{eff}}$) and ($k_{s,\text{eff}}$) represent the fluid and solid effective thermal conductivities, respectively.

Then, the governing Eqs. (1)–(5) are non-dimensionalised using the following groups of variables:

$$X, Y = \frac{x, y}{D_i}, \quad U = \frac{u D_i}{\alpha_f}, \quad V = \frac{v D_i}{\alpha_f}, \quad \theta = \frac{(T - T_c)}{(T_h - T_c)}, \quad P_f = \frac{p_f D_i^2}{\rho_f \alpha_f^2}, \quad (6)$$

here, (α_f) represents the thermal diffusivity. After that, the set of dimensionless governing equations becomes as follows:

$$\frac{\partial U}{\partial X} + \frac{\partial V}{\partial Y} = 0, \quad (7)$$

$$\frac{1}{\epsilon^2} \left(U \frac{\partial U}{\partial X} + V \frac{\partial U}{\partial Y} \right) = -\frac{\text{Pr}}{\text{Da}} U - \frac{C_F}{\sqrt{\text{Da}}} |\bar{U}| U + \frac{\text{Pr}}{\epsilon} (\nabla^2 U) - \frac{\partial P_f}{\partial X}, \quad (8)$$

$$\frac{1}{\epsilon^2} \left(U \frac{\partial V}{\partial X} + V \frac{\partial V}{\partial Y} \right) = -\frac{\text{Pr}}{\text{Da}} V - \frac{C_F}{\sqrt{\text{Da}}} |\bar{U}| V + \frac{\text{Pr}}{\epsilon} (\nabla^2 V) - \frac{\partial P_f}{\partial Y} + \text{Ra} \text{Pr} \theta_f, \quad (9)$$

$$\epsilon \left(U \frac{\partial \theta_f}{\partial X} + V \frac{\partial \theta_f}{\partial Y} \right) = \frac{k_{f,\text{eff},(x,y)}}{k_f} (\nabla^2 \theta_f) + \text{Bi} Kr (\theta_s - \theta_f), \quad (10)$$

$$\frac{k_{s,\text{eff}}}{k_s} (\nabla^2 \theta_s) - \text{Bi} (\theta_s - \theta_f) = 0, \quad (11)$$

where (U) and (V) represent the non-dimensional horizontal and vertical velocities, respectively, (X) and (Y) represent the non-dimensional system coordinates, (θ) is the non-dimensional temperature, and (P_f) is the non-dimensional pressure. In addition, it can be seen that there is a group of non-dimensional parameters appearing in Eqs. (7)–(11) represent the essential parameters for the current problem thus:

$$\text{Ra} = \frac{\rho_f g \beta D_i^3 (T_h - T_c)}{\alpha_f \mu_f}, \quad \text{Da} = \frac{K}{D_i^2}, \quad \text{Bi} = \frac{D_i^2 h_{sf} a_{sf}}{k_s}, \quad Kr = \frac{k_s}{k_f}. \quad (12)$$

In this study, the inertia coefficient (C_F) and the permeability (K) are calculated based on Ergun's empirical expressions Ergun [31], which are functions of particle diameter (d) and porosity (ϵ) as follows:

$$C_F = \frac{1.75}{\sqrt{150 \epsilon^3}}, \quad K = \frac{\epsilon^3 d^2}{150 (1 - \epsilon)^2}. \quad (13)$$

Whereas, the specific inter-phase surface area (a_{sf}) and the particle-to-air convective coefficient (h_{sf}) are calculated employing the empirical

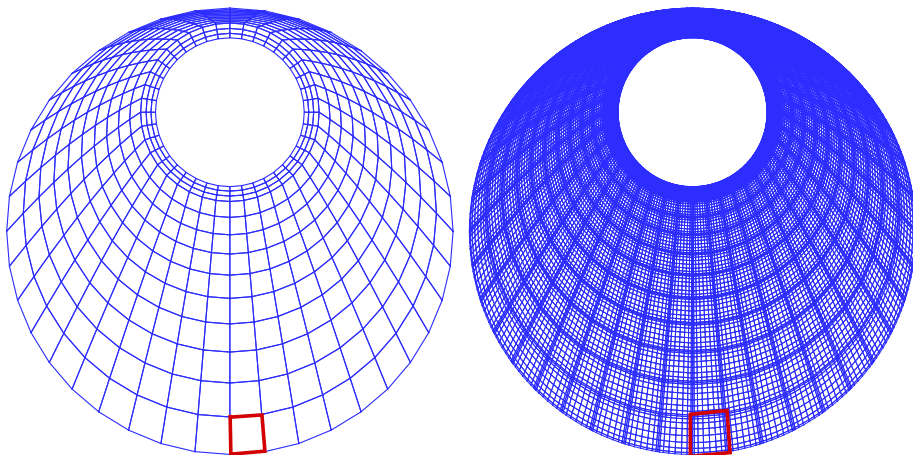


Fig. 2. (a) Macro-elements, and (b) micro-elements.

Table 1

Thermal conductivities (k_s) of number of solid non-metallic and metallic substrates, showing their thermal conductivity ratios with respect to air ($k_f = 0.02587 \text{ W/m K}$ at 300 K).

Non-metals	k_s (W/m K)	k_s/k_f	Metals	k_s (W/m K)	k_s/k_f
foam	0.026	1.005	lead	35	1.352×10^3
rubber	0.138	5.33	steel	50	1.932×10^3
wood	0.17	6.57	nickel	62	2.396×10^3
crystal	0.2	7.73	iron	79	3.053×10^3
brick	0.47	18.1	brass	144	5.566×10^3
soil	0.5	19.3	bronze	189	7.305×10^3
concrete	0.8	30.9	aluminium	237	9.161×10^3
window glass	1.0	38.6	Silicon carbide	270	1.043×10^4
Silica	1.07	41.3	aluminium nitride	310	1.198×10^4
Quartz	1.4	54.1	gold	315	1.217×10^4
Chalk	2.2	85.04	copper	385	1.488×10^4
Zircon	2.44	94.3	silver	429	1.658×10^4
carbon	6.92	267.4	diamond	2100	0.811×10^5

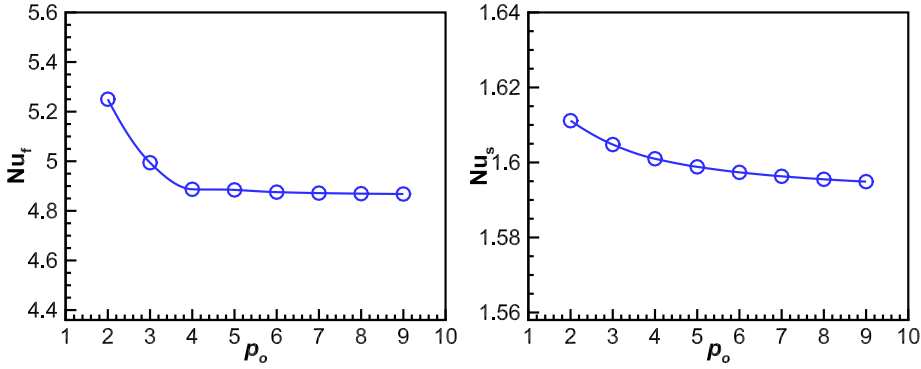


Fig. 3. Results of mesh resolution study showing the variation of (Left) Nu_t and (Right) Nu_s , with polynomial order p_o .

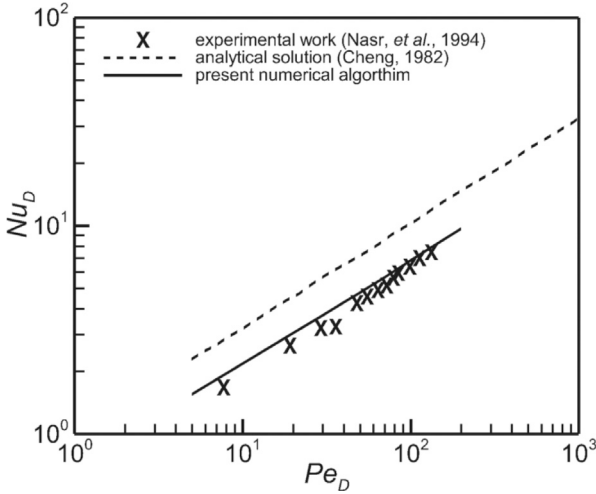


Fig. 4. Comparison between the results of the present numerical algorithm and analytical results of Cheng [27] and experimental results of Nasr et al. [9].

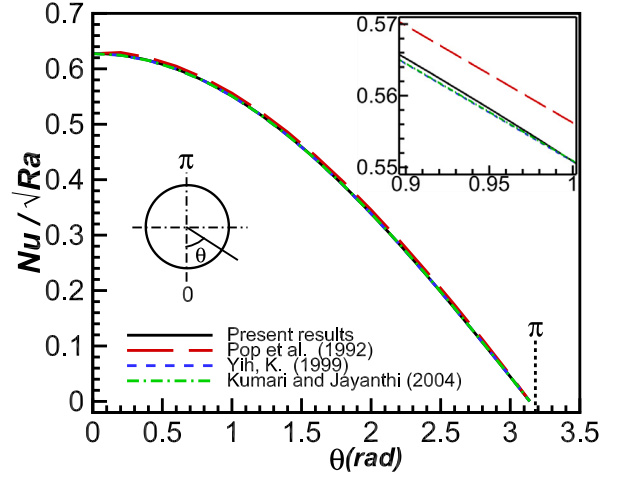


Fig. 5. Comparison between the results of the present numerical algorithm and the results of Pop et al. [28], Yih [29] and Kumari and Jayanthi [30].

formulations of Dullien [32] and Wakao et al. [33], respectively, as follows:

$$a_{sf} = \frac{6(1-\epsilon)}{d}, \quad (14)$$

$$h_{sf} = \frac{k_f}{d} \left(2 + \text{Pr}^{1/3} \text{Re}_p^{0.6} \right), \quad (15)$$

here, (Re_p) is the particle Reynolds number in the pore scale,

$$\text{Re}_p = \frac{\rho_f |v| d}{\mu_f}. \quad (16)$$

Therefore, by substituting Eqs. (13)–(16) into Eq. (12), importantly, Biot and Darcy numbers become functions of porosity ϵ , cylinder/particle diameter ratio (D_i/d), and solid/fluid thermal conductivity ratio Kr , as follows:

$$\text{Bi} = 6(1-\epsilon) \left(\frac{1}{Kr} \right) \left(\frac{D_i}{d} \right)^2 \left(2 + (\text{Pr})^{1/3} (\text{Re}_p)^{0.6} \right). \quad (17)$$

$$\text{Da} = \left(\frac{d}{D_i} \right)^2 \frac{\epsilon^3}{150(1-\epsilon)^2}, \quad (18)$$

In addition, the another important factor that should be taken into account is the dispersion conductivity (k_d). This factor is considered as

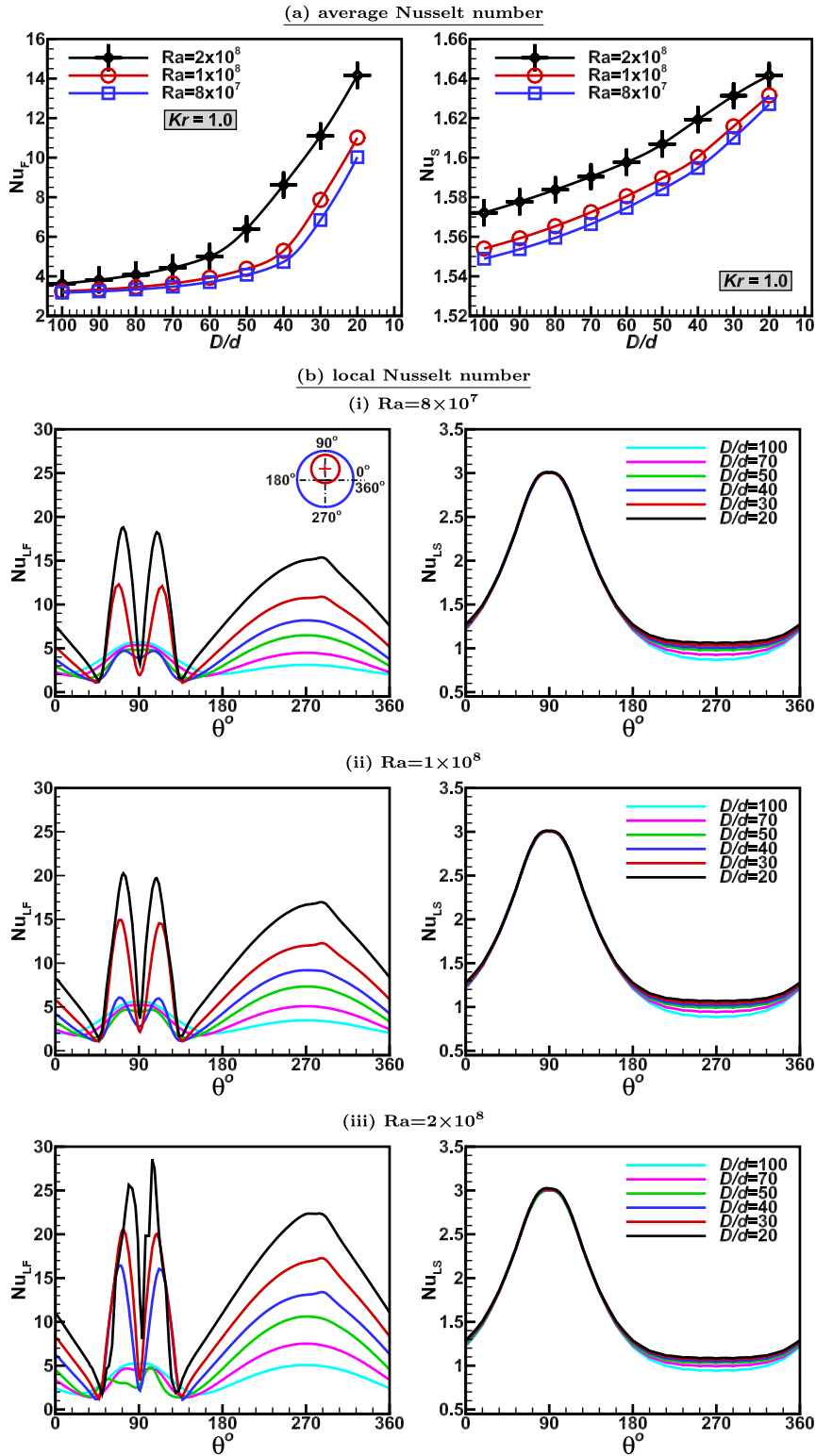


Fig. 6. (a) Variations of (Left) Nu_F and (Right) Nu_S with D_i/d at different Ra , at $Kr = 1.0$. (b) Variation of (Left column) Nu_{LF} and (Right column) Nu_{LS} around the cylinder circumference for different D_i/d and Ra , at $Kr = 1.0$ and $\varepsilon = 0.5$.

an additional diffusive part appended to the stagnant thermal connectivity of fluid in both longitudinal and lateral directions. The empirical correlations developed by Wakao and Kaguei [34] are used to model

the fluid dispersion conductivities as follows:

$$\frac{k_{d,(x)}}{k_f} = 0.5 \operatorname{Pr} \operatorname{Re}_p, \quad (19)$$

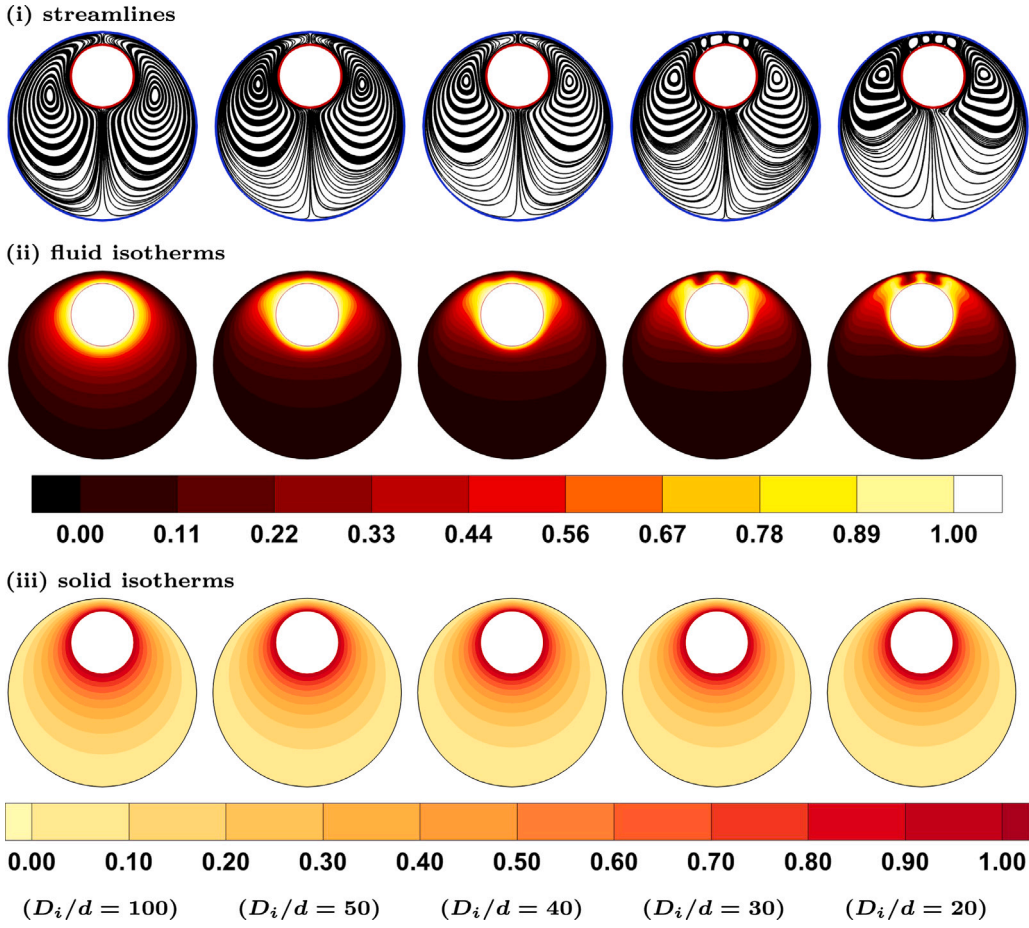


Fig. 7. Samples of (i) streamlines, (ii) fluid isotherms, and (iii) solid isotherms, for different particle diameters, at $Kr = 1.0$, $\epsilon = 0.5$, and $Ra = 8 \times 10^7$.

$$\frac{k_{d,(y)}}{k_f} = 0.1 \operatorname{Pr} \operatorname{Re}_p. \quad (20)$$

While, the experimental correlations of Zehner and Schluender [35] are considered to calculate the fluid and solid stagnant conductivities, as follows:

$$\frac{k_{st,f}}{k_f} = \left(1 - \sqrt{1 - \epsilon}\right) + \left(\frac{2\sqrt{1 - \epsilon}}{1 - \lambda B}\right) \left(\frac{(1 - \lambda)B}{(1 - \lambda B)^2} \ln(\lambda B) - \frac{B + 1}{2} - \frac{B - 1}{1 - \lambda B}\right), \quad (21)$$

$$\frac{k_{st,s}}{k_s} = (1 - \epsilon), \quad (22)$$

where $\lambda = 1/Kr$ and $B = 1.25((1 - \epsilon)/\epsilon)^{\frac{10}{9}}$. Thereby, the fluid and solid effective thermal conductivities $k_{f,\text{eff}}$ and $k_{s,\text{eff}}$ in Eqs. (10) and (11) become calculated as follows:

$$\frac{k_{f,\text{eff},(x,y)}}{k_f} = \frac{k_{st,f}}{k_f} + \frac{k_{d,(x,y)}}{k_f}, \quad (23)$$

$$\frac{k_{s,\text{eff}}}{k_s} = \frac{k_{st,s}}{k_s}. \quad (24)$$

4. Boundary conditions and energy calculation

In the present study, the no slip condition is assumed for the dimensionless velocities on the two solid cylinders' walls, whereas, the

dimensionless temperatures on these walls are considered as follows:

$$\begin{aligned} \theta_f &= \theta_s = 1 & \text{at } (r = r_i) \text{ and } (0 < \varphi^\circ < 360), \\ \theta_f &= \theta_s = 0 & \text{at } (r = r_o) \text{ and } (0 < \varphi^\circ < 360). \end{aligned} \quad (25)$$

Moreover, Fourier's law is employed to calculate the quantity of heat transferred from the inner cylinder wall into the fluid and solid phases, as follows:

$$q_f = -\frac{k_{f,\text{eff}}}{k_f} \frac{\partial T_f}{\partial n}, \quad q_s = -\frac{k_{s,\text{eff}}}{k_s} \frac{\partial T_s}{\partial n}, \quad (26)$$

Thereafter, Eq. (26) is transformed to be in terms of dimensionless parameters as follows:

$$\begin{aligned} \text{Nu}_{LF} &= \frac{q_f D_i}{(T_h - T_c)} = -\frac{k_{f,\text{eff}}}{k_f} \frac{\partial \theta_f}{\partial n}, \\ \text{Nu}_{LS} &= \frac{q_s D_i}{(T_h - T_c)} = -\frac{k_{s,\text{eff}}}{k_s} \frac{\partial \theta_s}{\partial n}, \end{aligned} \quad (27)$$

where, (Nu_{LF}) and (Nu_{LS}) represent the local Nusselt numbers of fluid and solid phases, respectively, over the inner cylinder periphery. Then, the surface-average Nusselt numbers (Nu_F) and (Nu_S) are calculated by integrating the local Nusselt numbers along the inner cylinder circumference as follows:

$$\begin{aligned} \text{Nu}_F &= \frac{1}{S} \int_0^S \frac{k_{f,\text{eff}}}{k_f} \frac{\partial \theta_f}{\partial n} ds, \\ \text{Nu}_S &= \frac{1}{S} \int_0^S \frac{k_{s,\text{eff}}}{k_s} \frac{\partial \theta_s}{\partial n} ds, \end{aligned} \quad (28)$$

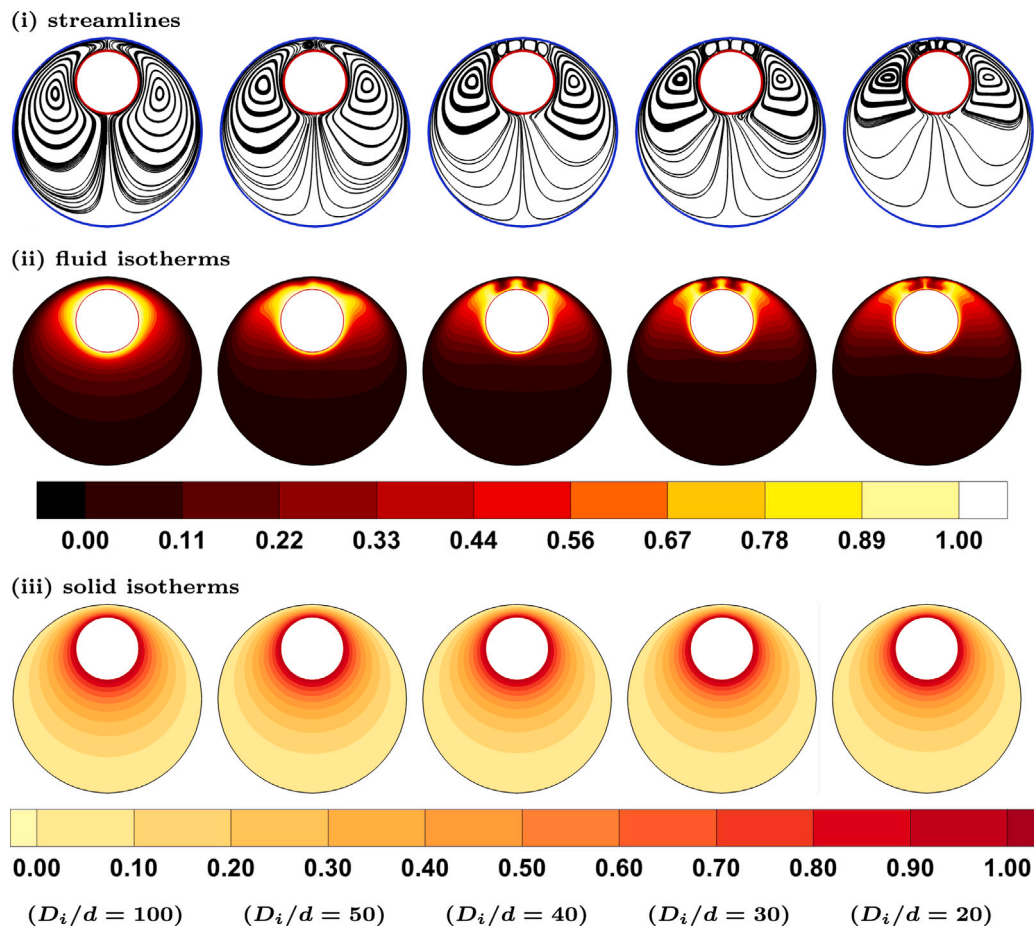


Fig. 8. Samples of (i) streamlines, (ii) fluid isotherms, and (iii) solid isotherms, for different particle diameters, at $Kr = 1.0$, $\epsilon = 0.5$, and $Ra = 2 \times 10^8$.

here (*n*) and (*s*) refer to the perpendicular and tangential orientations, respectively, at the wall of cylinder, while, (*S*) is the cylinder circumference.

5. Numerical approach

The spectral element method is employed to numerically solve the governing Eqs. (7)–(11) along with the boundary conditions in Eq. (25). This method, which is exhaustively explicated in Karniadakis et al. [36] and Thompson et al. [37], is inserted in our privately owned code to analyse unsteady free convection in a porous medium. In this approach, the partial differential equations are discretised spatially and temporally. Spatially, the Galerkin technique, which is a nodal-based spectral-element technique described in Fletcher [38,39] and Karniadakis and Sherwin [40], is employed to discretise the equations. Like that, the computational region is split into a number of rough unrefined quadrilateral macro-elements. This means that each macro-element contains four corner nodes. Fig. 2a demonstrates the macro-elements employed in the current investigation. It is comprised from 520 macro-elements and 560 nodes. During the integration process, these macro-elements use non-linear Lagrange polynomials as weighting and shape functions. Indeed, employing such polynomials enables every macro-element to be extra partitioned into $(N_x \times N_y)$ interior nodes for further mesh resolution and producing micro-elements or micro-mesh, as illustrated in Fig. 2b, which will be used in the numerical runs. Consequently, a mesh resolution study can be conducted by altering the order of the Lagrangian polynomial (*po*) to

secure that numerical results are independent to the size of the spatial mesh. Temporally, the explicit Adams–Bashforth approach is employed to discretise the advection term, while the implicit Adams–Moulton approach is used to discretise the diffusion and pressure terms. These two approaches are thoroughly described in Chorin [41], Karniadakis et al. [36] and Thompson et al. [37].

A mesh resolution study was performed by increasing the polynomial order within the range of (*po* = 2 – 9) to produce a typical micro-mesh for the numerical runs. Within this study, the average fluid and solid Nusselt numbers Nu_f and Nu_s are employed as accuracy indicators. Fig. 3 shows an example of the study results at Rayleigh number ($Ra = 5 \times 10^7$), annulus interior cylinder/sphere diameter ratio ($D_i/d = 30$), and porosity ($\epsilon = 0.5$). In this figure, it is shown that Nu_f and Nu_s are converged at *po* = 8 with an error of less than 0.1%. This means that a group of (9×9) interior nodes are used in every macro-element, as demonstrated in the red-marked element in Fig. 2.

The code algorithm was verified against analytical and experimental results of Cheng [27] and Nasr et al. [9], respectively. The verification was conducted for the problem of forced convection about a circular cylinder having a diameter of $D = 2.7$ mm, and submerged inside a packed bed of aluminium spheres having a diameter of $d = 12.23$ mm. Fig. 4 shows this comparison for the distributions of average Nusselt number (Nu_D) with Péclet number (Pe_D), and depicts a rational agreement. In addition, the precision of the present algorithm was also verified against the results of Kumari and Jayanthi [30], Pop et al. [28] and Yih [29], for the problem of natural convection about a circular cylinder immersed in a saturated porous medium. Fig. 5 demonstrates

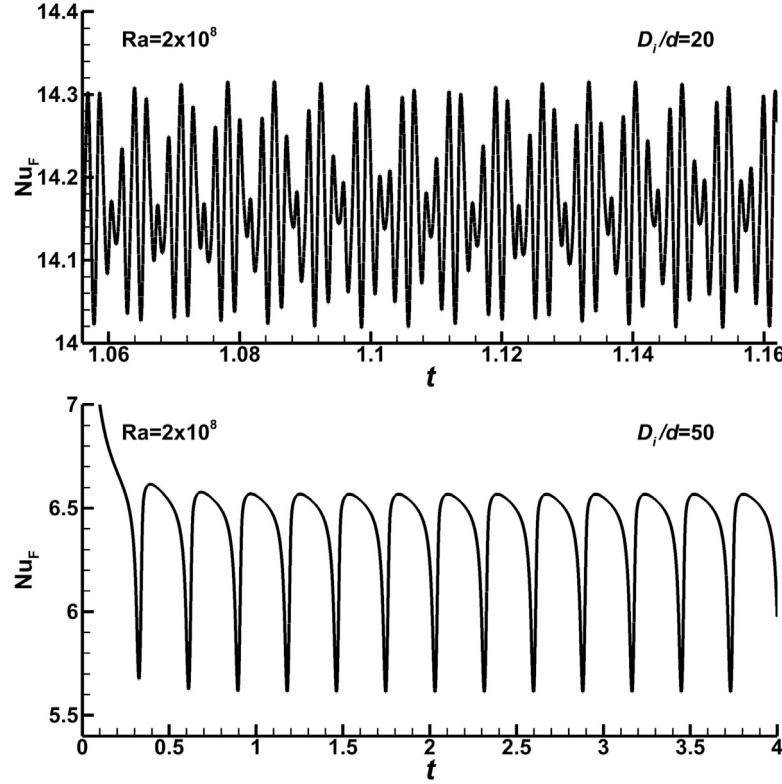


Fig. 9. Variation of Nu_F with time at (Top) $D_i/d = 20$, and (Bottom) $D_i/d = 50$, at $\text{Ra} = 2 \times 10^8$.

this comparison, and also shows a reasonable agreement with an error less than 0.05%. Furthermore, it is worth mentioning that our code was used and validated number of times priorly, for instance in Al-Sumaily et al. [42] and Al-Sumaily and Thompson [43] for forced convective flow over a cylinder in a porous medium, in Al-Sumaily [44] for forced convective flow over multi-cylinders in a porous medium, and in Al-Sumaily and Thompson [45] for natural convective flow around a cylinder in a porous enclosure.

6. Discussion the results

As mentioned before in the introduction that there have been some conflicting conclusions concerning the dependency of the convective heat transfer on the particle diameter d and the porosity ϵ of the porous medium used. Therefore, the present study focusses on this dependency as Rayleigh number and solid-to-fluid thermal conductivity ratio are varied. Indeed, the effects of these two independent pertinent parameters were investigated for the following ranges: Cylinder-to-particle diameter ratio ($D_i/d = 100 - 20$) and porosity ($\epsilon = 0.3 - 0.7$). Here, it is worth mentioning that in Eq. (6) (Normalisation), the inner cylinder diameter was taken as the unit scale ($D_i = 1.0$); therefore within the range of the particle diameter, it can be seen that when the ratio of D_i/d decreases from 100 to 20, this means that the particle diameter d increases. The results were obtained at three different values of Rayleigh number ($\text{Ra} = 8 \times 10^7, 1 \times 10^8, 2 \times 10^8$), and for solid-to-fluid thermal conductivity ratio ($Kr = 1 - 10^5$) covering a broad range of non-metallic and metallic porous substrates as air was chosen to be the flowing fluid with ($\text{Pr} = 0.71$) and ($k_f = 0.025 \text{ W/m.K}$), as demonstrated in Table 1.

6.1. Effect of particle diameter

Fig. 6 shows the effect of particle diameter on the convection heat transfer throughout the fluid phase (average and local fluid Nusselt numbers Nu_F , Nu_{LF} , respectively) and the conduction heat transfer throughout the solid phase (average and local solid Nusselt numbers Nu_S , Nu_{LS} , respectively), at different Rayleigh numbers, and at $Kr = 1.0$, e.g., very low solid thermal conductivity k_s for non-metallic materials, and at $\epsilon = 0.5$. It can be clearly seen that as the particle diameter d increases, e.g., D_i/d decreases, both the average fluid and solid Nusselt numbers Nu_F and Nu_S increase. It is shown that the increase in Nu_F becomes great at higher Rayleigh numbers, i.e., $\text{Ra} = 2 \times 10^8$. Also, the increase in Nu_F becomes sharp at lower particle diameters, i.e., $D_i/d < 50$. The reason is that the convection heat transfer is intensified when the thermal dispersion k_d increases. The empirical expressions of the thermal dispersion k_d , given in Eqs. (19) and (20), display that this parameter is a strong function of the particle diameter and the fluid velocity v ; thus it increases as anyone of these two variables increases. Therefore, firstly, increasing Rayleigh number leads to an increase in the convective flow currents and the flow velocity in the vicinity of the cylinder wall. Thus, at low and moderate values of $\text{Ra} \leq 10^8$, the fluid velocity in the pore scale is not strong, and the added dispersive conductivity developing from the enlargement in the particle diameter is not sufficiently great to raise k_d extremely. However, at high values of $\text{Ra} > 10^8$, the impact of k_d becomes greater, and the convection heat transfer enhances considerably as the particle diameter enlarges. Additionally, the figure shows that the average conductive Nusselt number Nu_S slightly increases with increasing the particle diameter. The reason will be discussed in detail later. However, importantly, the comparison between the plots of the figure demonstrates that the overall change in Nu_F at any d is more significant than that in Nu_S .

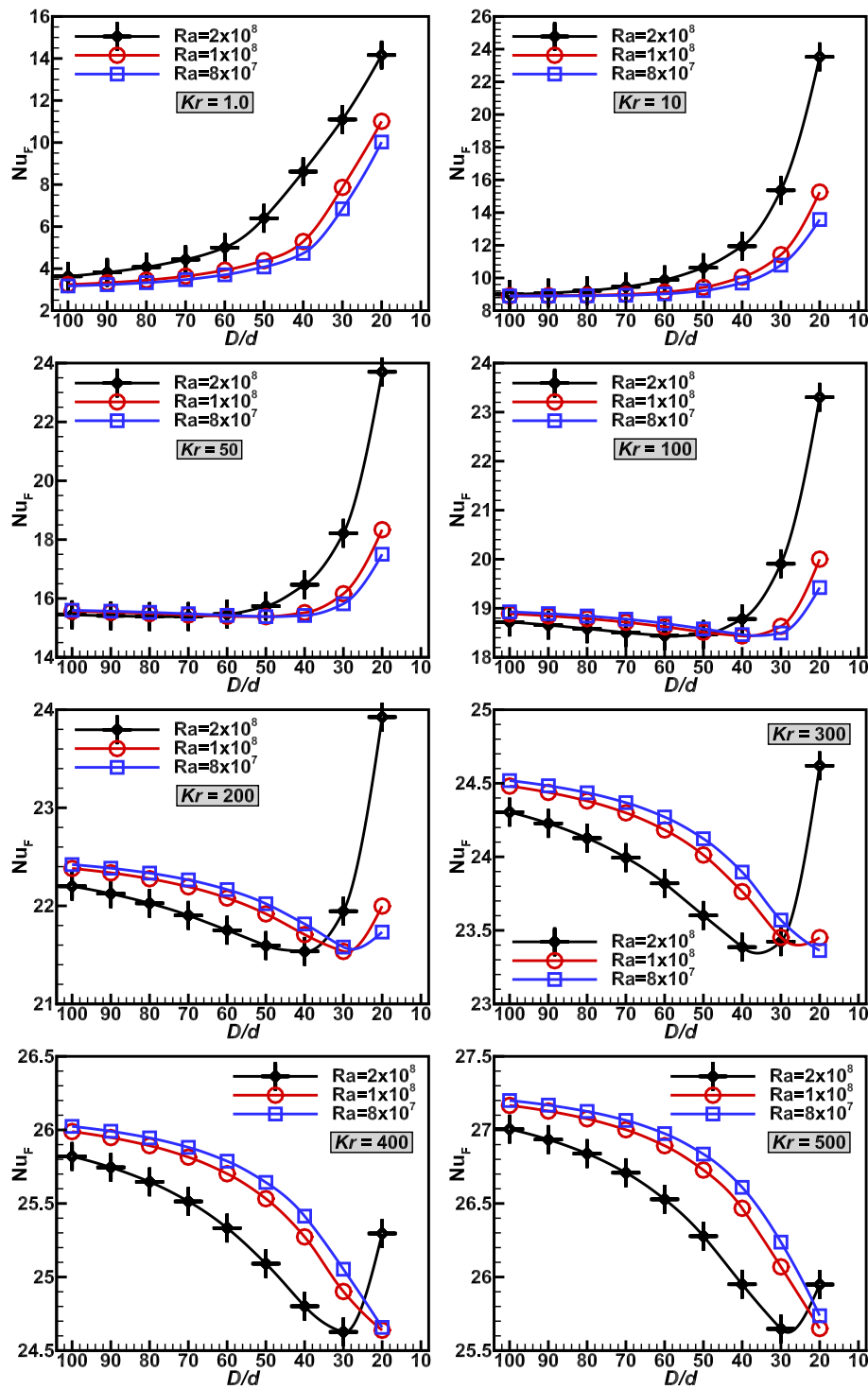


Fig. 10. Variations of Nu_F with D_i/d at different Ra, and at various solid/fluid thermal conductivity ratio ranging between $Kr = 1 - 10^5$.

for all Ra. Furthermore, the figure shows different distributions for the local fluid and solid Nusselt numbers Nu_{LF} and Nu_{LS} , respectively, with angular positions around the cylinder surface. This is because that the fluid thermal boundary layer around the heated cylinder surface is highly affected by the flow speed within the hydrodynamic boundary layer of the fluid. Thus, the regions that experience high flow speed produce high local fluid temperature gradients, and then generate higher Nu_{LF} as at $\theta = 70^\circ$, $\theta = 100^\circ$, $\theta = 270^\circ$ for higher particle

diameter. Whereas, the solid thermal boundary layer around the heated cylinder surface is hardly and not directly influenced by the flow speed. It is shown that the distribution of Nu_{LS} is only affected at $\theta = 90^\circ$ because the solid thermal boundary layer is compressed by the gap between the cylinders and not by the flow velocity. It is obvious in the next Figs. 7 and 8.

Moreover, the influence of the particle diameter on the flow conduct and the fluid and solid temperature fields within the annular space,

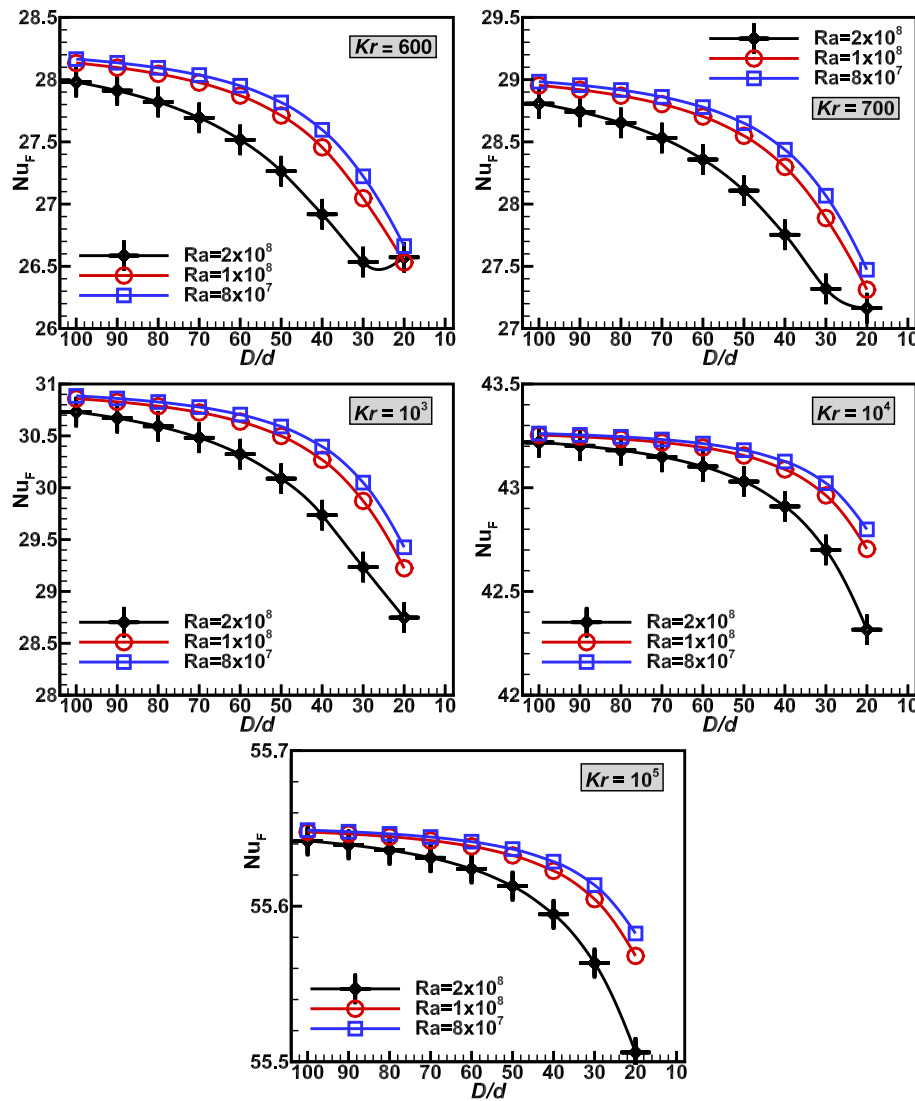


Fig. 10. (continued).

are shown in Figs. 7 and 8 at $\text{Ra} = 8 \times 10^7$ and $\text{Ra} = 2 \times 10^8$, respectively, and at fixed $Kr = 1.0$ and $\epsilon = 0.5$. It can be seen that at low particle diameters $D_i/d \geq 40$, the flow conduct in the annular space is completely a unicellular flow. Thus, there is only one pair of cells, which rotate opposite to each other on the left and right sides of the interior cylinder. The intensity of these cells increases and they move upward as the particle diameter increases. This is due to that when the particle size is small, the amount of solid material becomes large, therefore, the movement of the fluid within the solid phase becomes highly restricted, generating insignificant free convection. However, by increasing the particle diameter $D_i/d \leq 30$, the fluid flow becomes easier to penetrate the solid particles as the void fraction is increased due to the enlargement in the pore spaces between the particles. This produces higher free convection in the area, converting the unicellular flow into multicellular flow, i.e., generating three pairs of cells at $D_i/d = 30$ and 20. This action becomes more significant for higher

Rayleigh number $\text{Ra} = 2 \times 10^8$, demonstrated in Fig. 8, as the multicellular flow conduct begins earlier at $D_i/d = 40$. It is worth mentioning here that in some cases such as at $\text{Ra} = 2 \times 10^8$ and $D_i/d = 20$ and 50, the flow becomes unsteady (periodic), as illustrated in Fig. 9, showing oscillatory motions for the cells horizontally above the interior cylinder. This can be apparently seen in the plots of streamlines in Fig. 8 at $D_i/d = 20$, which depicts the clear non-uniform unstable cells' movement and the deformation in the cells' shapes occurring due to

this oscillatory movement. Moreover, the plots in Figs. 7 and 8 display that the decrease in the particle diameter tends to magnify the thermal boundary layers of fluid and solid phases surrounding the cylinder. The isotherms of both phases appear to be analogous at smaller particle diameter d , which refers to the condition of thermal equilibrium in the bed. But, it can be seen that the variance between the two temperature fields develops as the particle diameter or Rayleigh number increases.

It is necessary to investigate the influence of the particle diameter on heat transfer within porous beds at different low, moderate and high solid thermal conductivities. In another word, to investigate the influence of porous thermal conductivity on the reliance of heat transfer on the particle diameter. For this purpose, Fig. 10 displays the variations of Nu_F with particle diameter D_i/d , at variant solid/fluid thermal conductivity ratios ranging between $Kr = 1 - 10^5$ covering most of the non-metallic, semi-metallic, and metallic porous materials, and at different Rayleigh numbers. It can be seen that the effect of particle size for the non-metallic beads on Nu_F is entirely different from that for the metallic beads. Thus, when using highly non-metallic porous materials, the plots reveal that Nu_F increases as the particle size enlarges. However, this trend of Nu_F changes gradually into the whole negative impact at higher solid thermal conductivity for highly metallic porous materials. To clarify the reasons of these attitudes, it is important to know that there are three mechanisms of heat transfer occurring in the system. The first mechanism is the convection heat

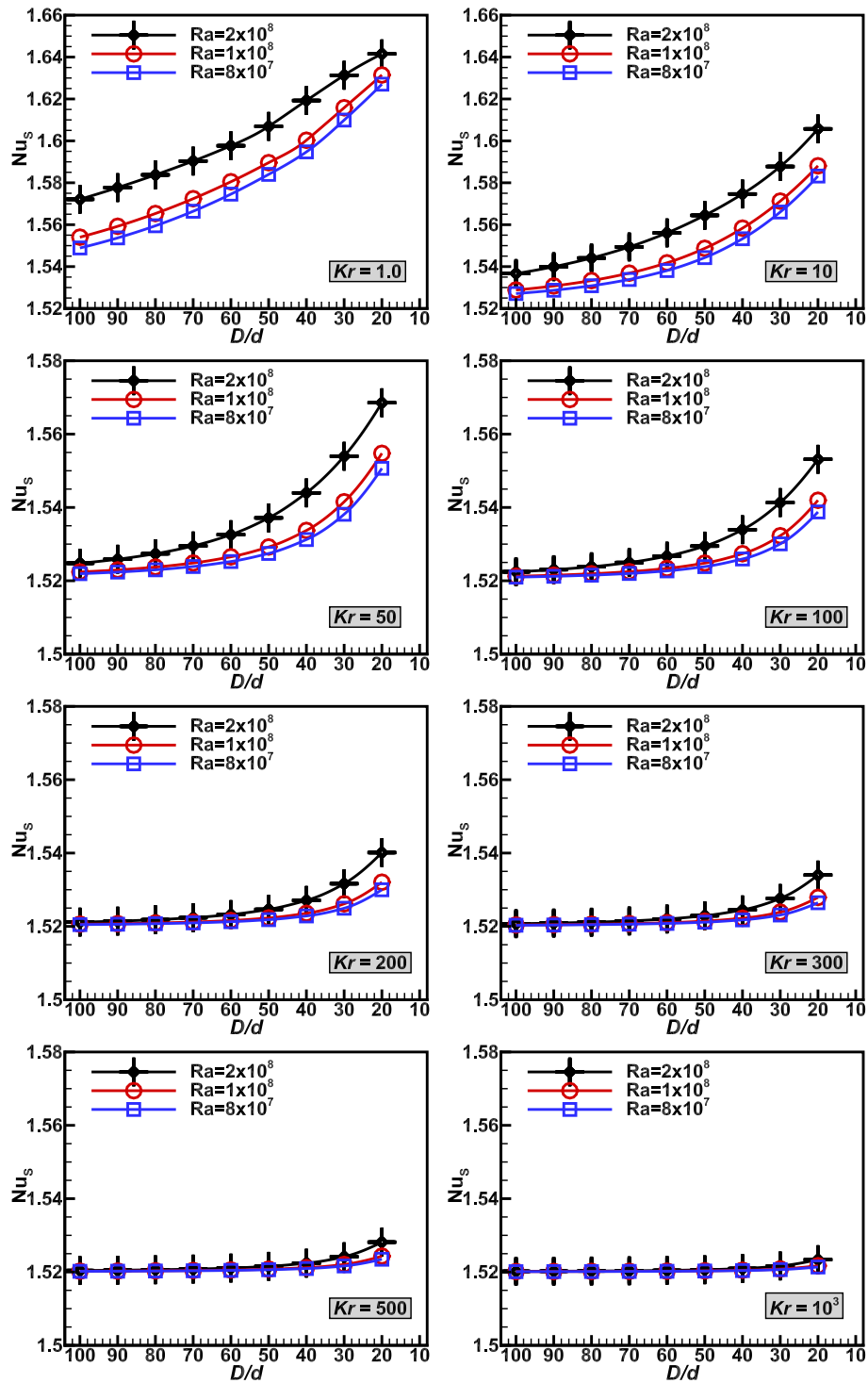


Fig. 11. Variations of Nu_s with D_i/d at different Ra , and at various solid/fluid thermal conductivity ratio ranging between $Kr = 1 - 10^3$.

transferred from the hot inner cylinder directly into the fluid phase. This mechanism is a function of the fluid thermal conductivity and the contact surface area "CSA" between the heated cylinder and the solid particles. The second mechanism is the conduction heat transferred from the hot cylinder directly into the solid particles touching it. This mechanism is a function of the solid thermal conductivity as well as the contact surface area "CSA" between the heated cylinder and

the solid particles. The third mechanism is the interfacial convection heat transfer between the particles and the surrounding fluid, which is called in the literature as the "*fin effect*". Indeed, this effect is a complicated mechanism as it is a function of five parameters, namely the inter-phase surface area of the particles a_{sf} in Eq. (14), the particle-to-fluid convective heat transfer coefficient h_{sf} in Eqs. (15) and (16), the dispersive thermal conductivity in Eqs. (19) and (20), the porous

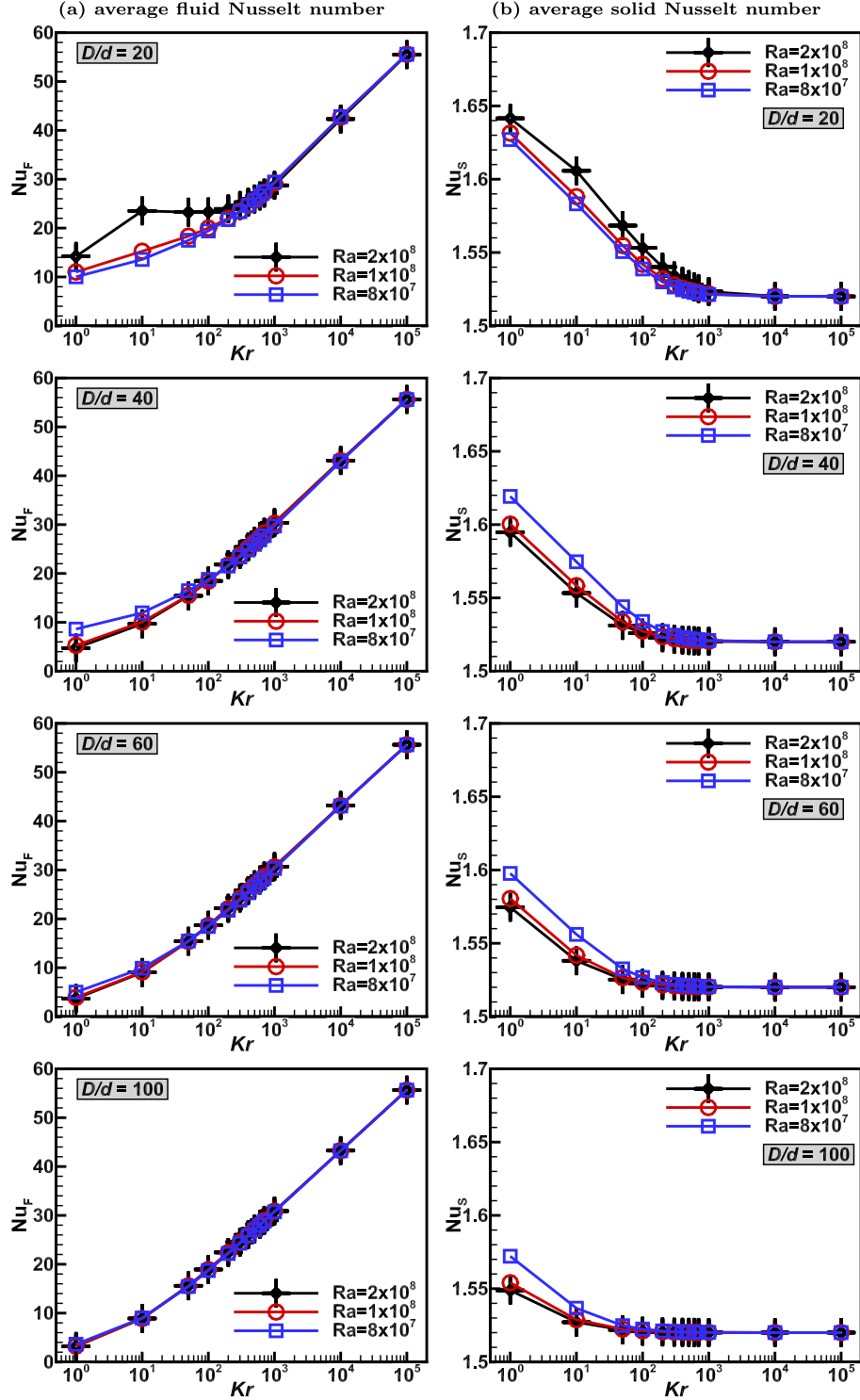


Fig. 12. Trends of (a) Nu_F and (b) Nu_S , with Kr at variant Ra and D_i/d .

permeability in Eqs. (13) and (18), and the amount of conduction heat released from the solid particles to the surrounding fluid.

Firstly, at low solid thermal conductivity k_s , the conduction heat transfer during the particles is poor owing to the high conductive thermal resistance. Thereby, the majority of the heat transports directly into the fluid phase by convection. Also, increasing the particle diameter

causes a decrease in the contact surface area “CSA” between the hot cylinder and the solid particles decreases; however, the hot surface area exposed to the flowing fluid is increased, producing higher values of Nu_F . This is directly. Indirectly, in this case, the “fin effect” becomes acting to transfer heat from the fluid phase into the solid particles. Then, as the particle diameter enlarges, the interfacial convective heat

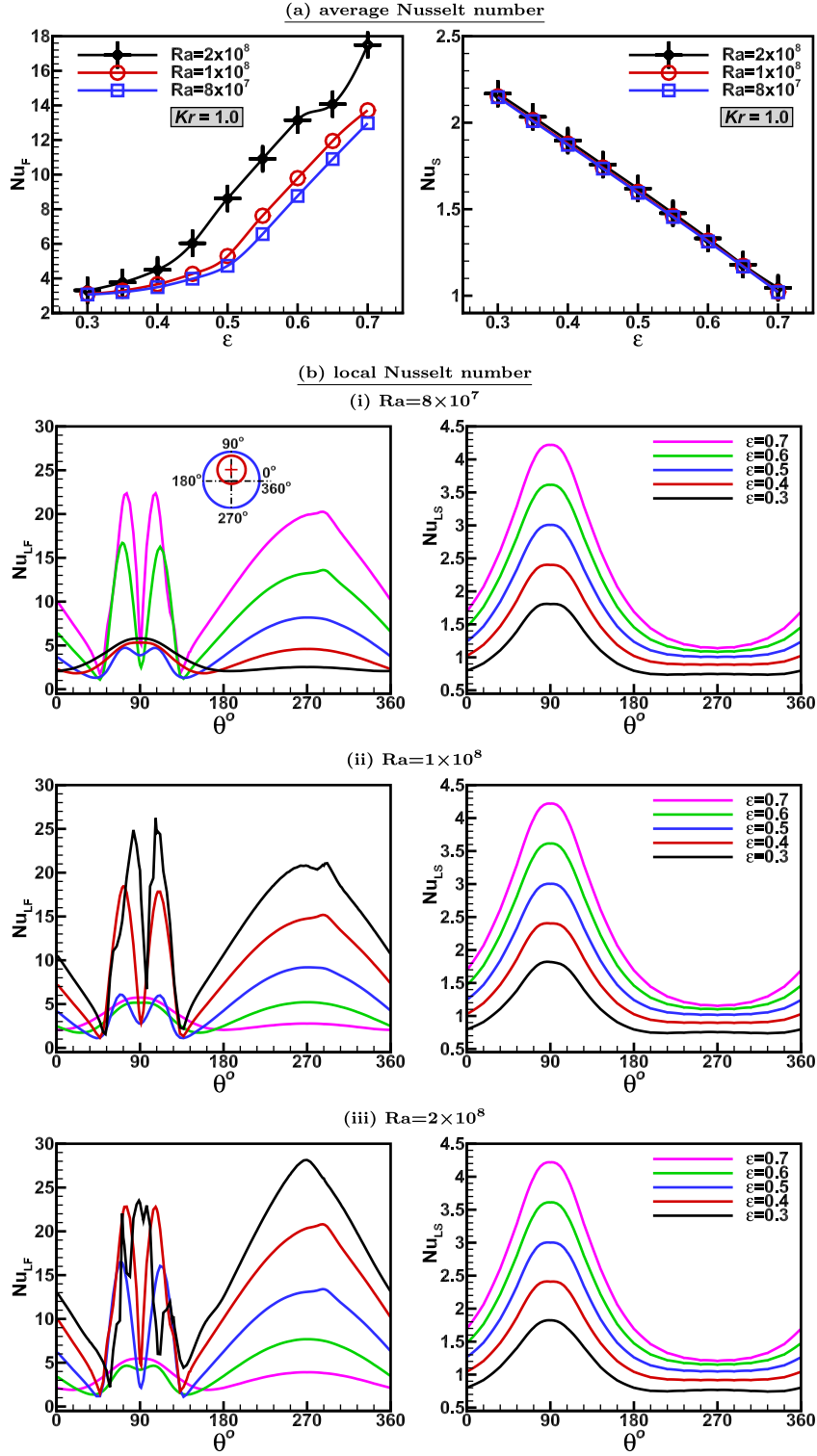


Fig. 13. (a) Variations of (Left) Nu_F and (Right) Nu_S with ϵ at different Ra , and (b) Variation of (Left column) Nu_{LF} and (Right column) Nu_{LS} around the cylinder circumference for different ϵ and Ra , both at $Kr = 1.0$ and $D_i/d = 40$.

transfer coefficient h_{sf} in Eqs. (15) and (16), and the dispersive thermal conductivity in Eqs. (19) and (20), are also increased. This leads to a further and significant increase in Nu_F due to the enlargement in the particle diameter.

Secondly, however, by increasing the solid/fluid thermal conductivity ratio to be between $Kr = 50 - 100$, representing using semi-metallic porous materials, the conduction heat transfer within the solid phase is improved, increasing the solid field temperatures. Consequently, the

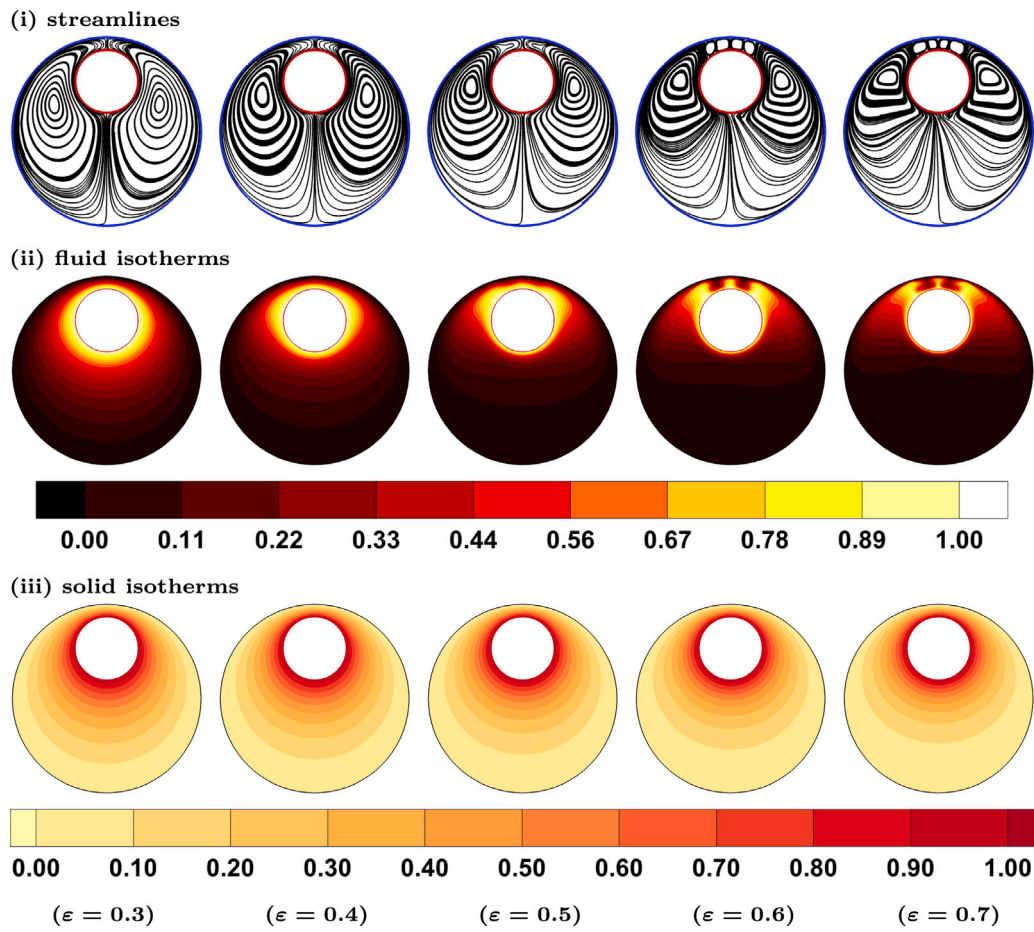


Fig. 14. Samples of (i) streamlines, (ii) fluid isotherms, and (iii) solid isotherms, for different porosity, at $Kr = 1.0$, $D_i/d = 40$, and $Ra = 8 \times 10^7$.

fluid-to-particles “fin effect” becomes weaker, resulting in a remarkable decrease in the effect of the particle size on Nu_F , particularly at small particle sizes. Lastly, further increase in the solid/fluid thermal conductivity ratio, i.e., $Kr \geq 100$, causes a more increase in the conduction heat transfer during the particles, and a more decrease in the direct convection into the fluid phase. This produces a higher reversed (particles-to-fluid) “fin effect”. Thereby, as the particle diameter increases, although the hot surface area exposed to the fluid phase increases, the bigger effect of the reversed “fin effect” is also enhanced, resulting in a raising in the fluid temperature field. Then, this obviously leads to a remarkable reduction in Nu_F as the particle diameter increases.

Indeed, these findings for the effect of particle diameter on Nu_F at different kind of porous particle beads, e.g., different k_s , in free convection regime at higher Rayleigh numbers are similar to those reported by Al-Sumaily et al. [46] in forced convection at higher Reynolds numbers.

Moreover, Fig. 11 shows the variations of Nu_S with particle diameter D_i/d , at variant solid/fluid thermal conductivity ratio within the range of $Kr = 1 - 10^3$. We mentioned above that at low solid thermal conductivity k_s , the conduction heat transfer becomes poor, and Nu_S decreases as the particle diameter increases. However, the plots of Fig. 11 show the opposite trend. Hence, it can be seen that Nu_S increases as the particle diameter increases for all solid thermal conductivities. But, it is shown that the effect of the particle diameter on the trends of Nu_S is significant only at lower k_s , and it diminishes at higher k_s .

The reason is that as the particle diameter increases, the particle-to-fluid convective heat transfer coefficient h_{sf} in Eqs. (15) and (16) is also increased. Consequently, the reversed (particles-to-fluid) “fin effect” increases too. Indeed, it seems that the heat transfer due to the reversed “fin effect” is higher than the direct reduction in Nu_S . Therefore, this significant contribution from the reversed “fin effect” causes a decrease in the temperature field within the solid particles. As a result, the solid thermal boundary layer is decreased and the solid temperature gradient around the heated cylinder is increased, leading to an increase in Nu_S . However, at very higher k_s , as the particle diameter enlarges, it is obvious that the significant increase in the conduction heat transfer during the particles owing to the higher k_s balances the reduction in the conduction heat transfer as a result of the particle diameter enlargement as well as the increased reversed “fin effect” together.

Fig. 12 displays the variations of Nu_F and Nu_S with the thermal conductivity ratio Kr , at different Rayleigh numbers and particle sizes. One can see that the increase in Kr increases Nu_F and decreases Nu_S . It is shown that the increase in Nu_F is significant and becomes linear after $Kr \geq 100$. However, the decrease in Nu_S becomes trivial after $Kr \geq 100$. Also, the increments of Nu_F are much higher than the decrements of Nu_S . This is due to the effective fluid thermal conductivity is highly influenced by changing Kr .

6.2. Effect of porosity

Fig. 13 shows the effect of porosity on the average and local fluid Nusselt numbers Nu_F and Nu_{LF} , respectively, and on the average and

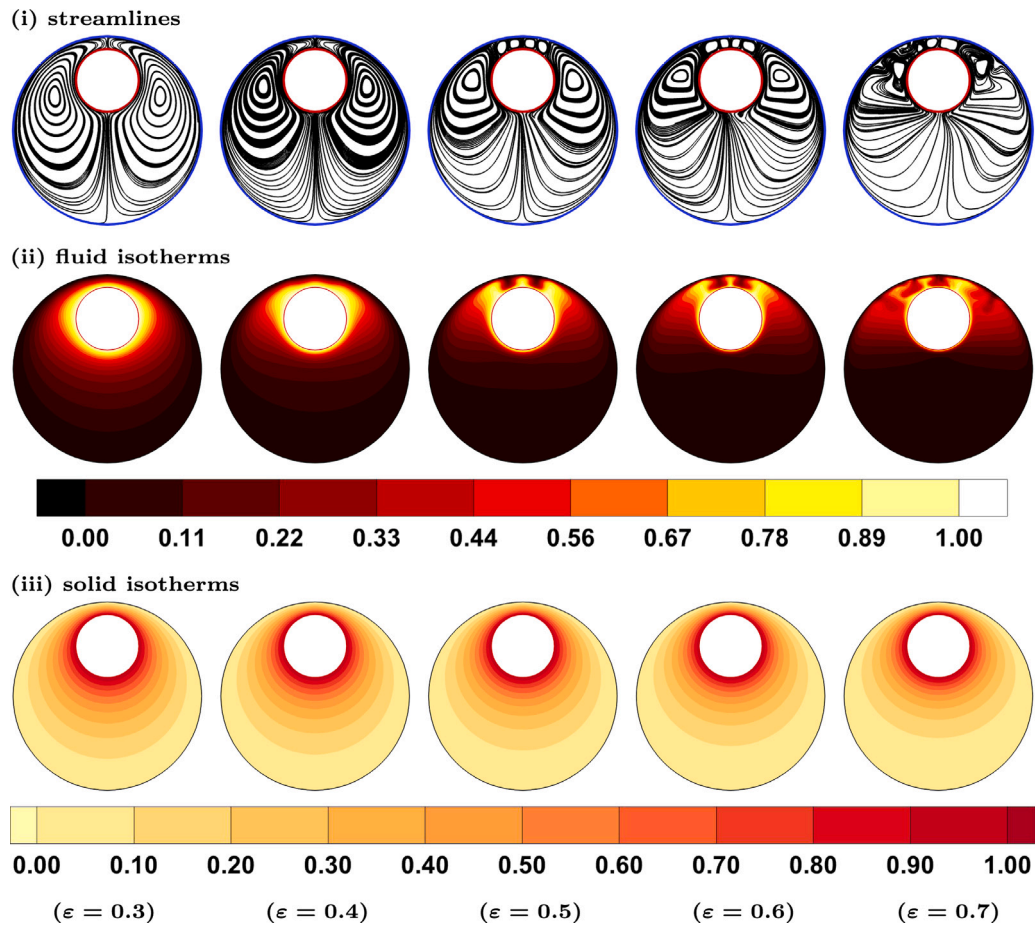


Fig. 15. Samples of (i) streamlines, (ii) fluid isotherms, and (iii) solid isotherms, for different porosity, at $Kr = 1.0$, $D_i/d = 40$, and $Ra = 2 \times 10^8$.

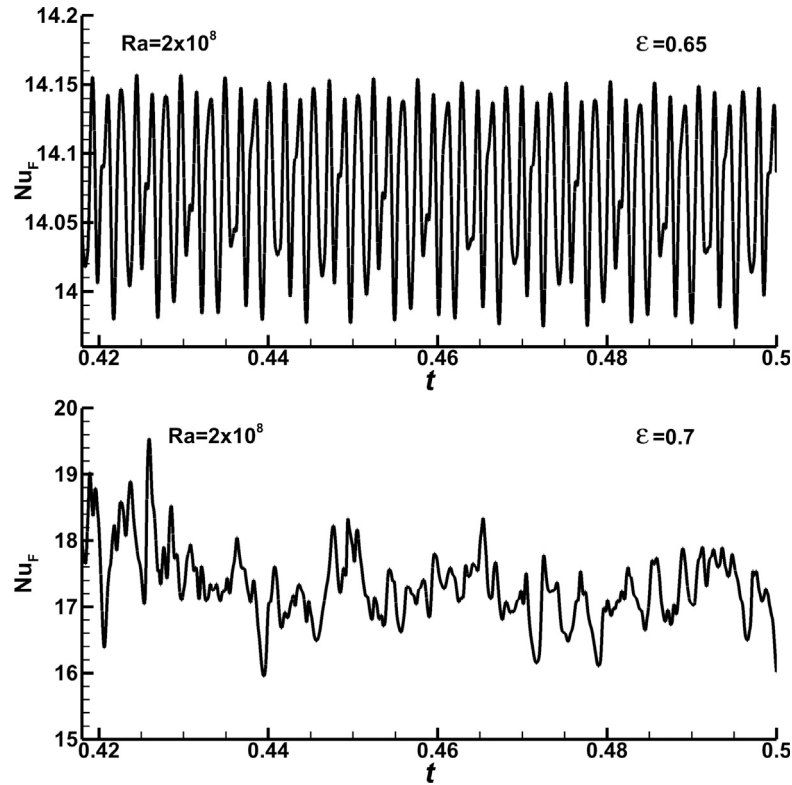
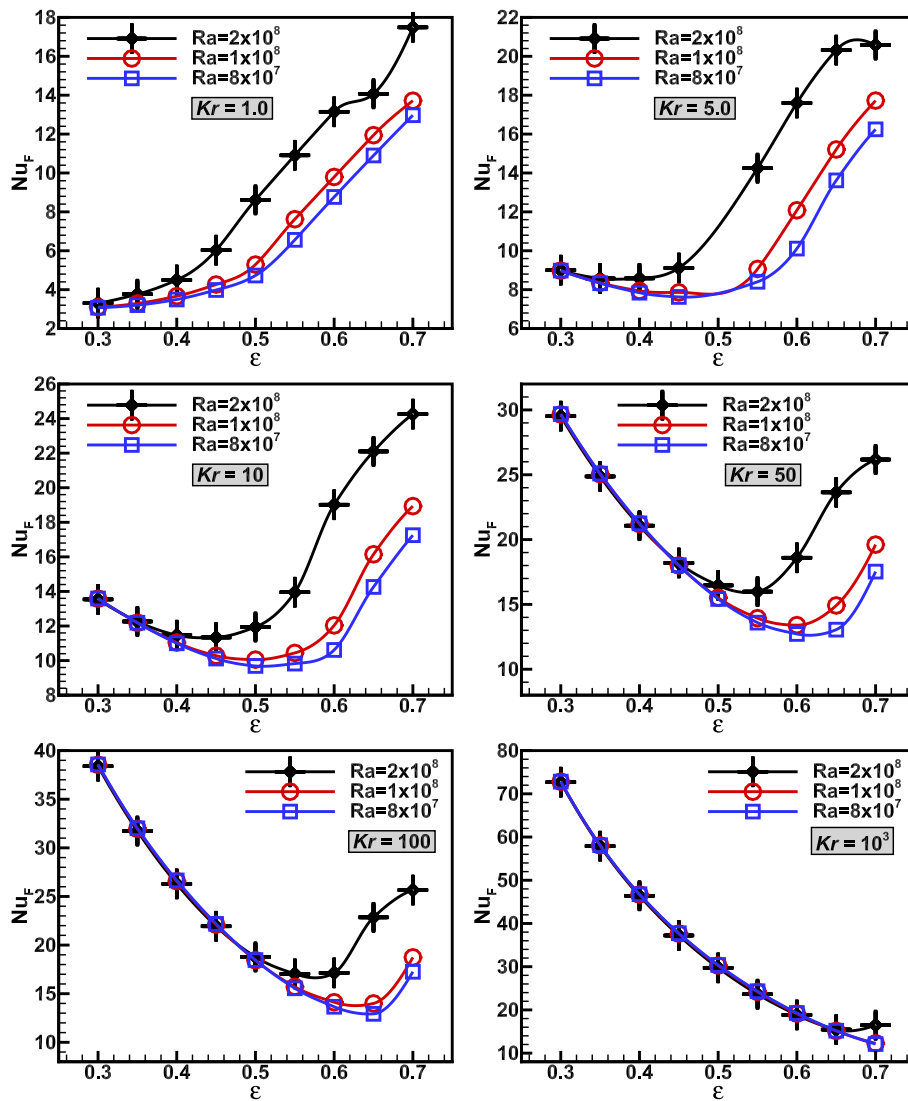


Fig. 16. Variation of Nu_F with time at (Top) $\epsilon = 0.65$, and (Bottom) $\epsilon = 0.7$, at $Ra = 2 \times 10^8$.

Fig. 17. Variations of Nu_F with porosity at different Ra and Kr .

local solid Nusselt numbers Nu_S and Nu_{LS} , respectively, at different Rayleigh numbers, and at constant $Kr = 1.0$ and $D_i/d = 40$. It is observed that the increase in the porosity enhances Nu_F and Nu_{LF} numbers; but decreases Nu_S and Nu_{LS} numbers. The reason will be discussed in detail later, but briefly can say that high porosity condition means a lower solid material exists within the porous medium, leading to a reduction in the contact surface area "CSA" between the heated cylinder and the solid particles. Therefore, as the porosity increases, the direct convection from the hot cylinder into the fluid phase increases; while, the direct conduction from the hot cylinder into the solid phase decreases. In addition, by comparing Figs. 6 and 13, one can see that the effect of porosity on Nu_F and Nu_S is higher than the effect of particle diameter. For example, it can be seen that at $Ra = 2 \times 10^8$ and $Kr = 1.0$, the increase in the porosity from $\epsilon = 0.3$ to 0.7 increases the value of Nu_F from 3.31 to 17.48 with 81% enhancement in convection heat transfer; while Nu_S decreases from 2.16 to 1.04 with 52% diminution in conduction heat transfer. Whereas, as the particle diameter increases from $D_i/d = 100$ to 20, Nu_F increases from 3.63 to 14.16 with 74.3% enhancement in heat transfer, but Nu_S decreases from 1.57 to 1.64 with 4.2% diminution in heat transfer.

The effect of changing the porosity value of the packed bed on the fluid flow and the thermal behaviour within both phases in the annular space, are shown in Figs. 14 and 15 at $Ra = 8 \times 10^7$ and $Ra = 2 \times 10^8$,

respectively, and at constant $Kr = 1.0$ and $D_i/d = 40$. Similar to the influence of the particle diameter, it is seen that at low porosity $\epsilon \leq 0.5$, the flow behaviour in the annular space is a unicellular flow by generating only one pair of cells. Also, the strength of the cells increases and they move upward as the porosity increases. This is attributed to that when the porosity is low, the void fraction is decreased owing to the reduction in the pore space between the particles. Therefore, the flow moves hardly within the solid phase producing weak free convection. Nevertheless, by increasing the porosity $\epsilon \geq 0.6$, the movement of the fluid flow becomes easier and generating higher free convection. It can be seen that the higher convection due to the higher porosity converts the unicellular flow into a multicellular flow, for example, three pairs of cells for $\epsilon \geq 0.6$. Also, this action becomes more significant for higher Rayleigh number $Ra = 2 \times 10^8$, demonstrated in Fig. 15, as the multicellular flow behaviour commences earlier at $\epsilon = 0.5$ instead of $\epsilon = 0.6$ at $Ra = 8 \times 10^7$. It can be seen that any change in porosity alters considerably the fluid temperature distribution around the inner cylinder, especially near the cylinder wall within the thermal boundary layer. So, it is found that the increase in porosity increases the distances between isothermal contour lines above the inner cylinder making a thermal plume touching the ceiling of the bed and moving along with it downwards. But, the solid temperature distribution seems to be hardly affected by any change in porosity of the porous medium. Also, the

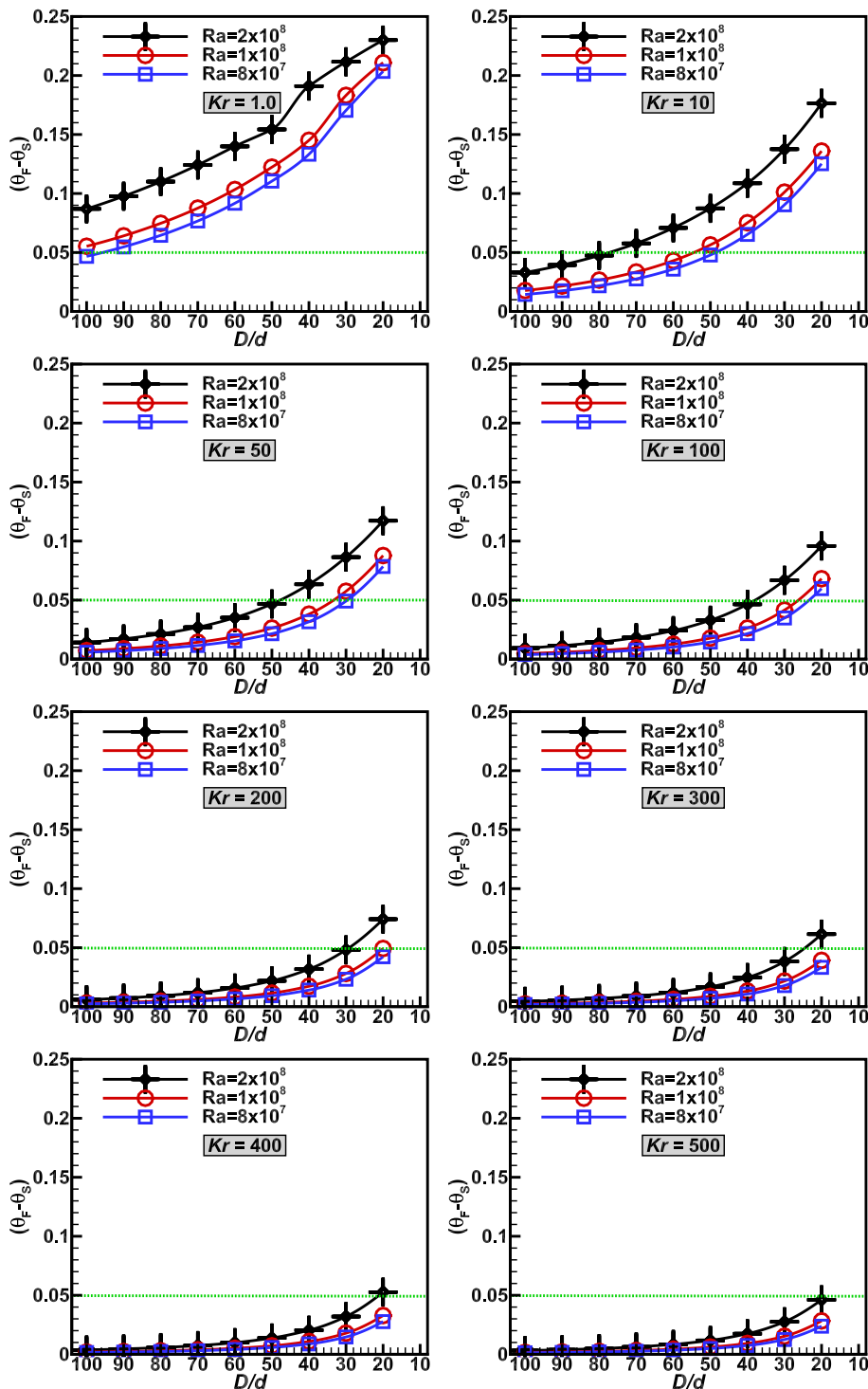


Fig. 18. Influence of particle diameter on the average temperature differential between the fluid and solid phases at different Kr and Ra .

isotherms of the two phases are shown to be similar at smaller ϵ , which refers to the thermal equilibrium condition in the bed. It is worth mentioning that in some cases at higher Rayleigh number $Ra = 2 \times 10^8$ and higher porosity $\epsilon = 0.65$ and 0.7, chaotic periodic flows are seen, see Fig. 16.

The effect of the porosity on Nu_F at different solid/fluid thermal conductivity ratios Kr is also investigated. Fig. 17 shows the variations of Nu_F with porosity at variant solid thermal conductivities $Kr = 1 - 10^3$, and at different Rayleigh numbers. It is observed that at $Kr = 1.0$,

as the porosity increases, Nu_F increases. However, interestingly, this behaviour changes to a decrease-increase trend at $5.0 \leq Kr \leq 10^2$ with a minimum point, for all Rayleigh numbers. But, these minimum points shift with ϵ as Kr increases, altering the trend of Nu_F into a continuous decrease one at higher $Kr \geq 10^3$. This is a very intricate behaviour and needs profound clarifications. Returning back to the three mechanisms of heat transfer aforementioned that control the entire thermal system, it can be stated that at $Kr = 1.0$, the conduction during the particles is poor, and the “fin effect” is performing from the fluid to the particles.

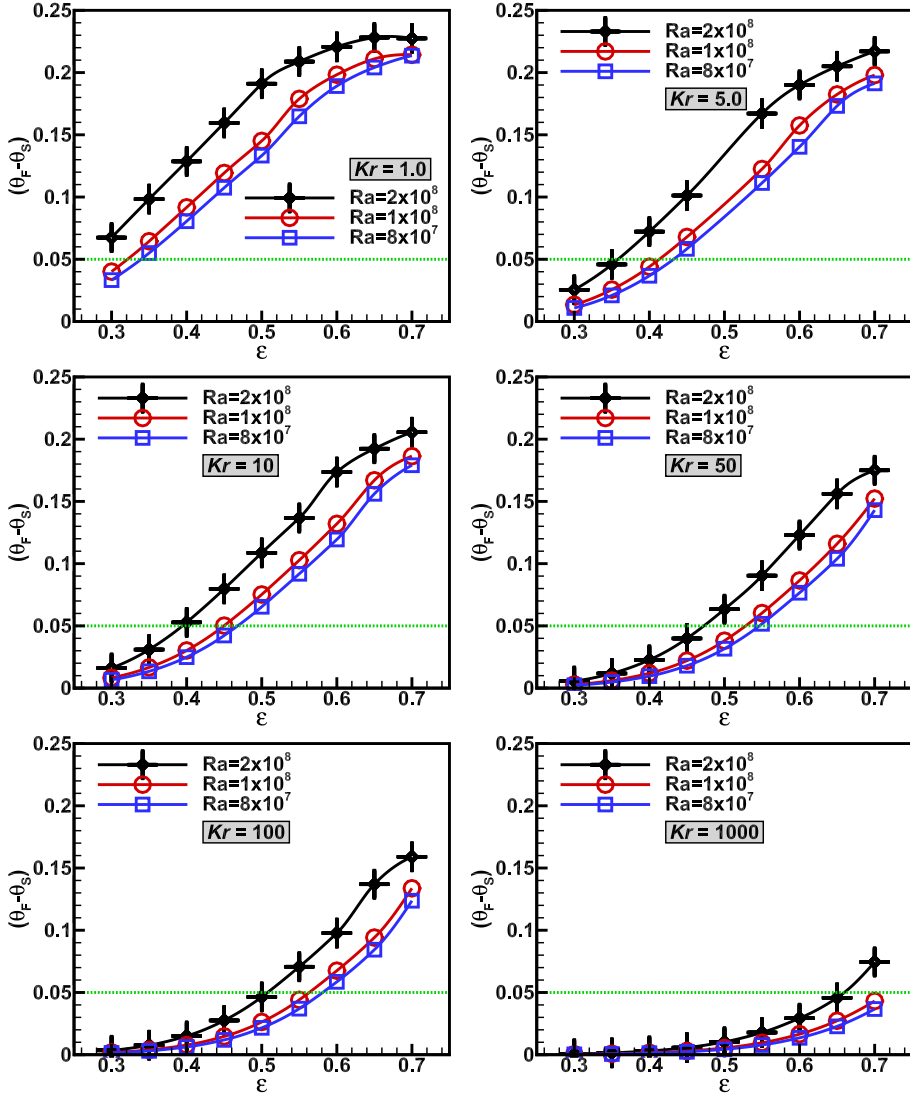


Fig. 19. Influence of porosity on the average temperature differential between the fluid and solid phases at different Kr and Ra .

Also, increasing the porosity causes three effects as follows; smaller inter-phase surface area a_{sf} , smaller “CSA”, but higher permeability K in Eq. (13). The first effect decreases the energy exchange (“fin effect”) between the two phases, causing a decrease in Nu_F . However, the second and third effects enlarge the hot cylinder surface area disclosed straightway to the fluid, resulting in a considerable direct increase in Nu_F , which appears to be much greater than the reduction because of the former impact.

Moreover, for $Kr > 1.0$, the immediate conduction into the particles increases, and the “fin effect” starts acting from the particles to the fluid. Therefore, as the porosity increases but in lower values, it seems that the impact of “fin effect” is still higher than the trivial direct convection, transferring more energy into the fluid from the particles. Thereby, it is seen that Nu_F decreases. However, further increase in the porosity making the direct convection effect to be predominant, causing Nu_F to increase. But, at higher $Kr \geq 1000$, the immediate conduction with the particles and the “fin effect” becomes very significant, and dominates the increased direct convection as the porosity increases. Thereby, it is seen that Nu_F continuously decreases. It is also observed

in Fig. 17 that the effect of Rayleigh number on Nu_F diminishes entirely at very lower values of porosity of $\epsilon = 0.3$.

6.3. Effects of particle diameter and porosity on “LTE” condition

Local thermal equilibrium “LTE” condition supposes that the variance between the fluid and solid phases’ temperatures of a porous medium is neglected everywhere and at any instant, see Al-Sumaily et al. [47]. This means that both phases have almost similar temperatures during the bulk porous system, and the radiative and convective heat transfer between the involved phases is ignored. Indeed, numerically, this implies that merely a single-phase energy equation is required to estimate the temperature field through the porous medium; however, not for per singular phase. Frankly, this approach simplifies solving the intricate highly-coupled governing formulations, and shortens the computational time. Therefore, it is important to assess the validity of the “LTE” assumption against the parameters prevailing the physical system. Abdedou and Bouhadef [48], Al-Sumaily et al. [49,50] used the *Local Thermal non-Equilibrium “LTNE”* energy model to calculate the temperatures of both fluid and solid phases and the average

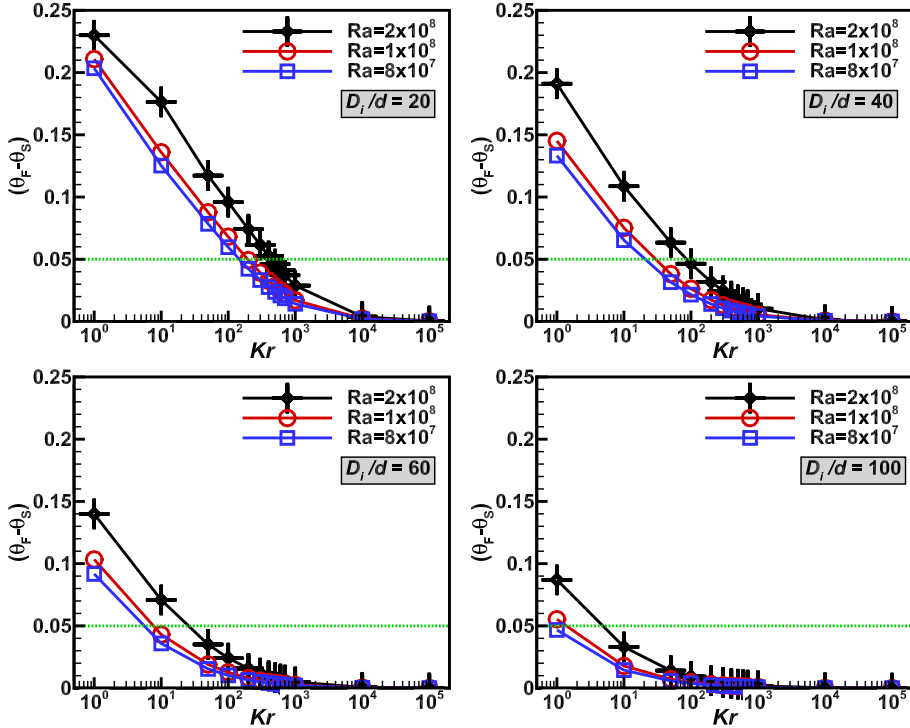


Fig. 20. Influence of thermal conductivity ratio on the average temperature differential between the fluid and solid phases at different D_i/d and Ra.

temperature difference between them throughout the entire computational domain. They pointed to that the “LTE” condition can be satisfied when the average temperature difference is less than or equal to 0.05. Following them, the variations of the average temperature difference between both phases ($\theta_F - \theta_S$) against the change in particle diameter, porosity, and thermal conductivity ratio are displayed in Figs. 18, 19, 20, respectively, at different Rayleigh numbers. It can be seen that the decrement in Rayleigh number, particle diameter, and/or porosity, or the increment in the thermal conductivity, have the tendency to reduce ($\theta_F - \theta_S$) and satisfy the “LTE” condition.

As mentioned above that the decrement in the particle diameter reduces a_{sf} and the “fin effect”, but increases “CSA” and the immediate conduction heat transfer during the particles. In consequence, this action allows the thermal fluid field to grow and get closer to the slightly altering thermal solid field, reducing ($\theta_F - \theta_S$), as illustrated in Fig. 19. This is clearly displayed in Fig. 21 at $Kr = 50$, representing the patterns of the local temperature difference between the two phases within the whole annular domain at different particle diameters. In addition, in Fig. 19, it is also seen that the porosity affects the ($\theta_F - \theta_S$) positively as a result of the elimination of solid substance from the porous medium, especially in the vicinity of the heated inner cylinder. Actually, increasing the removal of solid substance causes the heat amount transferred into the fluid phase to be much higher than that passed into the solid phase, producing higher phase temperature differential, as demonstrated in Fig. 22 at $Kr = 50$. It is worth mentioning that the impacts of porosity and particle diameter on the phase temperature differential becomes more pronounced at lower thermal conductivity ratio, see Figs. 21 and 22 at $Kr = 1.0$. It is important to notice that the influences of Rayleigh number, particle diameter, porosity, and thermal conductivity ratio in the current study are agreed with the results of Al-Sumaily et al. [50] for natural convection over a circular cylinder submerged in a square packed bed. However, they are opposite to the performance of particle diameter and the porosity

in the implementation of forced convection about a cylinder immersed in a horizontal bed presented by Al-Sumaily et al. [49].

7. Conclusions

In the present study, a two-dimensional unsteady free convection heat transfer inside an eccentric annular packed bed of spherical particles is numerically investigated. Numerical results are obtained to show the effect of the structural properties of the packed bed, i.e., the particle diameter and the porosity, for different values of Rayleigh number and porous materials (solid thermal conductivities) on the convection and conduction heat transfer. The main conclusions of the present analysis are presented as follows:

1. Generally, the effect of particle diameter on the average fluid Nusselt numbers Nu_F depends strongly on the solid thermal conductivity as follows: At low thermal conductivity ratio $Kr \leq 10$, Nu_F increases as the particle diameter increases. At mild $50 \leq Kr \leq 100$, Nu_F is a strong function of the particle diameter; thus, it can be increased or decreased at the particle diameter changes. Whereas, at higher $Kr \geq 100$, Nu_F decreases as the particle diameter increases.
2. Similarly, the effect of porosity on Nu_F relies on the solid thermal conductivity as follows: At low $Kr = 1.0$, Nu_F increases as the porosity increases. At moderate $5.0 \leq Kr \leq 100$, Nu_F decreases with the porosity for a minimum value, and then start increasing. These minimum values shift with porosity as Kr increases. While, at higher $Kr \geq 100$, Nu_F is decreased as the porosity increases.
3. Importantly, the effect of porosity on Nu_F and Nu_S is higher than the effect of particle diameter.
4. Interestingly, the effect of Rayleigh number on Nu_F is also dependent on the value of Kr as well as the particle diameter. Thus, Nu_F is increased as Ra increases at low Kr ; however, it is decreased as Ra increases at higher Kr , whereas at moderate Kr , Nu_F can be increased or decreased relying on the value of particle diameter.

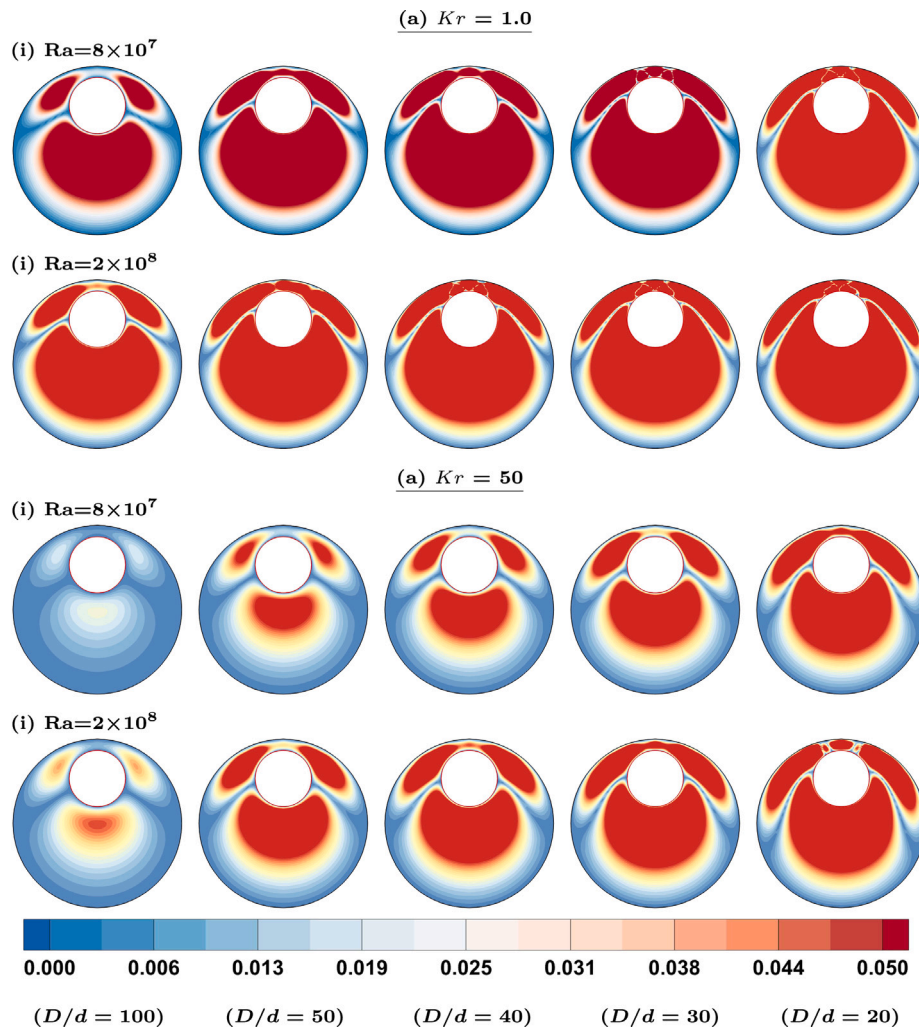


Fig. 21. Samples of temperature difference ($\theta_F - \theta_S$) within the annulus at different particle size (D_i/d), and at $\text{Ra} = 8 \times 10^7$ and 2×10^8 , and at $Kr = 1$ and 50 .

5. The increase in thermal conductivity ratio Kr increases Nu_F , but decreases Nu_S , for all values of Ra and particle diameter.
6. The decrease in Rayleigh number, particle diameter, and/or porosity, or the increase in the thermal conductivity ratio, have the tendency to reduce $(\theta_F - \theta_S)$ and satisfy the “LTE” condition.

Nomenclature

a_{sf}	specific interfacial area.
Bi	Biot number.
C_F	inertial coefficient.
d	particle diameter.
D_i	interior cylinder diameter.
D_o	exterior cylinder diameter.
Da	Darcy number.
h_{sf}	interfacial heat transfer coefficient.
k_f	thermal conductivity of fluid.
k_s	thermal conductivity of solid.
k_{st}	stagnant thermal conductivity of fluid.
Kr	solid/fluid thermal conductivity ratio.

K	permeability.
Nu	Nusselt number.
p_f	dimensional fluid pressure.
P_f	dimensionless fluid pressure.
Pr	Prandtl number.
Ra	Rayleigh number.
Re_p	Reynolds number in the pore scale.
S	circumference of the cylinder.
T	dimensional temperature.
u	dimensional horizontal velocity.
U	dimensionless horizontal velocity
v	dimensional vertical velocity.
V	dimensionless vertical velocity.
x, y	dimensional coordinates.
X, Y	dimensionless coordinates.

Greek symbols

ϵ	porosity.
θ	dimensionless temperature.
μ_f	dynamic viscosity.
ρ_f	density.
φ	angular coordinate.

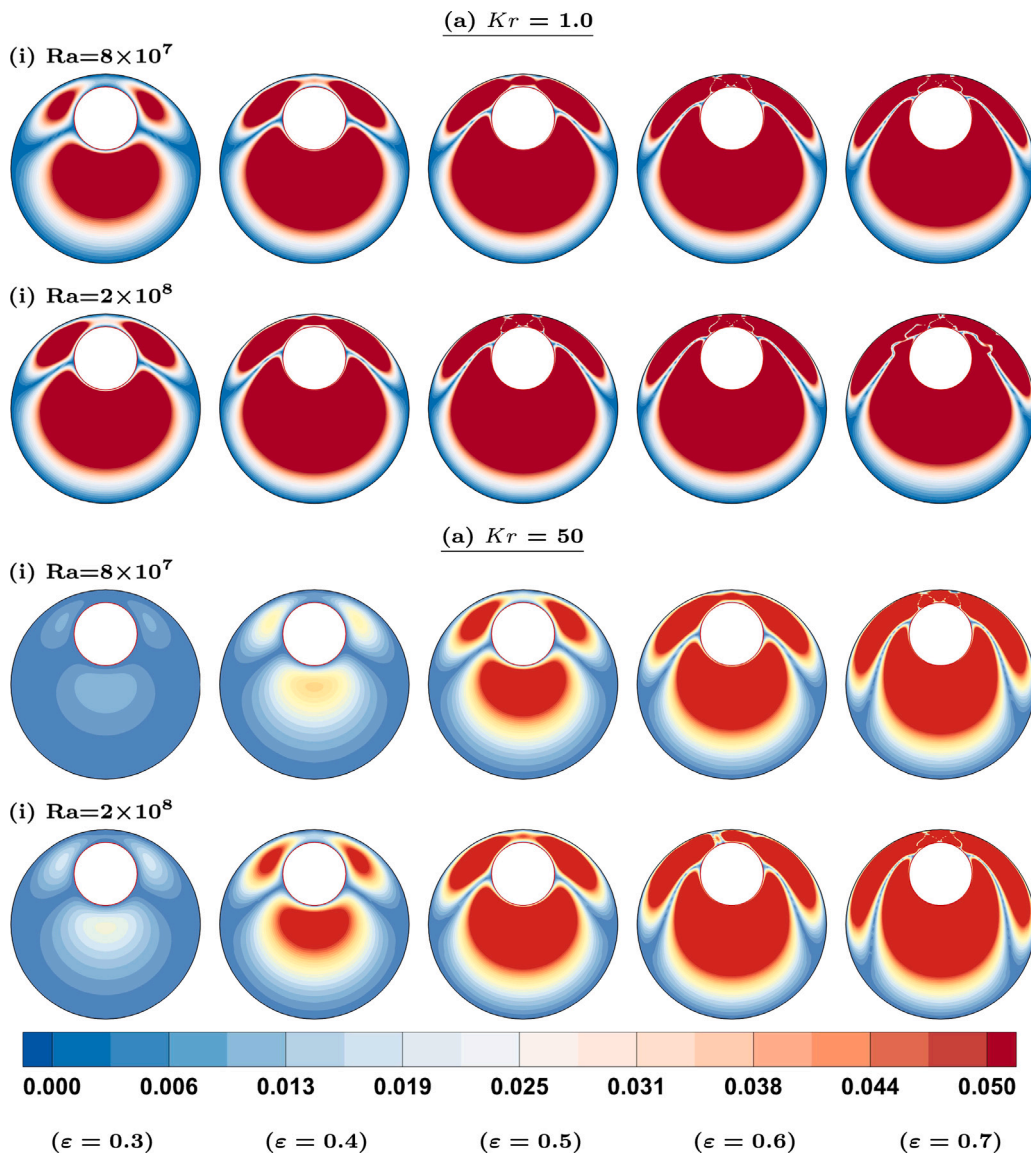


Fig. 22. Patterns of temperature difference ($\theta_F - \theta_S$) within the annulus at different porosity (ϵ), and at $Ra = 8 \times 10^7$ and 2×10^8 , and at $Kr = 1$ and 50 .

subscripts

eff	effective.
<i>f</i>	fluid.
<i>s</i>	solid.

Declaration of competing interest

The authors declare that they have no known competing financial interests or personal relationships that could have appeared to influence the work reported in this paper.

Data availability

Data will be made available on request.

Acknowledgements

This research was supported in part by the Monash eResearch Centre and eSolutions-Research Support Services through the use of the MonARCH HPC Cluster.

Funding

This research did not receive any specific grant from funding agencies in the public, commercial, or not-for-profit sectors.

References

- [1] E. Achenbach, Heat and flow characteristics of packed beds, *Exp. Therm Fluid Sci.* 10 (1995) 17–27.
- [2] G.L. David, P. Cheng, A numerical solution of variable porosity effects on natural convection in a packed -sphere cavity, *J. Heat Transfer* 113 (1991) 391–399.
- [3] N.J. Kwendakwema, R.F. Boehm, Parametric study of mixed convection in a porous medium between vertical concentric cylinders, *J. Heat Transfer* 113 (1991) 128–134.
- [4] S.W. Hsiao, P. Cheng, C.K. Chen, Non-uniform porosity and thermal dispersion effects on natural convection about a heated horizontal cylinder in an enclosed porous medium, *Int. J. Heat Mass Transfer* 35 (1992) 3407–3418.
- [5] B.X. Wang, J.H. Du, Forced convective heat transfer in a vertical annulus filled with porous media, *Int. J. Heat Mass Transfer* 36 (1993) 4207–4213.
- [6] P.X. Jiang, B.X. Wang, D.A. Luo, Z.P. Ren, Fluid flow and convective heat transfer in a vertical porous annulus, *Numer. Heat Transfer; Part A: Appl.* 30 (1996) 305–320.
- [7] U.A. Jeigarnik, F.P. Ivanov, N.P. Ikrankov, Experimental data on heat transfer and hydraulic resistance in unregulated porous structures (in Russian), *Teploenergetika* (1991) 33–38.

- [8] G.J. Hwang, C.H. Chao, Heat transfer measurement and analysis for sintered porous channels, *Trans. ASME. J. Heat Transf.* 116 (1994) 456–464.
- [9] K. Nasr, S. Ramadhyani, R. Viskanta, Experimental investigation on forced convection heat transfer from a cylinder embedded in a packed bed, *J. Heat Transfer* 116 (1994) 73–80.
- [10] G. Chen, H.A. Hadim, Numerical study of three-dimensional non-Darcy forced convection in a square porous duct, *Internat. J. Numer. Methods Heat Fluid Flow* 9 (1999) 151–169.
- [11] P.X. Jiang, G.S. Si, M. Li, Z.P. Ren, Experimental and numerical investigation of forced convection heat transfer of air in non-sintered porous media, *Exp. Therm Fluid Sci.* 28 (2004) 545–555.
- [12] M.B. Saito, M.J.S. Lemos, Laminar heat transfer in a porous channel simulated with a two-energy equation model, *Int. Commun. Heat Mass Transfer* 36 (2009) 1002–1007.
- [13] A. Blaszcuk, W. Nowak, J. Krzywanski, Effect of bed particle size on heat transfer between fluidized bed of group b particles and vertical rifled tubes, *Powder Technol.* 316 (2017) 111–122.
- [14] P.X. Jiang, Z.P. Ren, B.X. Wang, Z. Wang, Forced convective heat transfer in a plate channel filled with solid particles, *J. Therm. Sci.* 5 (1996) 43–53.
- [15] P.X. Jiang, Z. Wang, Z.P. Ren, B.X. Wang, Experimental research of fluid flow and convection heat transfer in plate channels filled with glass or metallic particles, *Exp. Therm Fluid Sci.* 20 (1999) 45–54.
- [16] G.F. Al-Sumaily, A. Nakayama, J. Sheridan, M.C. Thompson, The effect of porous media particle size on forced convection from a circular cylinder without assuming local thermal equilibrium between phases, *Int. J. Heat Mass Transfer* 55 (2012) 3366–3378.
- [17] T.C. Jue, Analysis of thermal convection in a fluid-saturated porous cavity with internal heat generation, *Heat Mass Transf.* 40 (2003) 83–89.
- [18] B.I. Pavel, An experimental and numerical study on heat transfer enhancement for gas heat exchangers fitted with porous media, *Int. J. Heat Mass Transfer* 47 (2004) 4939–4952.
- [19] M. Layeghi, A. Nouri-Borujerdi, Darcy model for the study of the fluid flow and heat transfer around a cylinder embedded in porous media, *Int. J. Comput. Methods Eng. Sci. Mech.* 7 (2006) 323–329.
- [20] Z.F. Huang, A. Nakayama, K. Yang, C. Yang, W. Liu, Enhancing heat transfer in the core flow by using porous medium insert in a tube, *Int. J. Heat Mass Transfer* 53 (2010) 1164–1174.
- [21] R. Mabrouk, H. Naji, H. Dahri, S. Hammouda, Z. Younsi, Numerical investigation of porosity effect on a pcms thermal performance in a porous rectangular channel via thermal lattice Boltzmann method, *Int. Commun. Heat Mass Transfer* 119 (2020).
- [22] X. Lu, Y. Zhang, S. Xiao, Y. Zhao, J. Li, J. Zhou, Q. Ouyang, Effect of structural characteristics on the natural convective heat transfer performance of copper foam, *Appl. Therm. Eng.* 204 (2022).
- [23] K.C. Wong, N.H. Saeid, Numerical study of mixed convection on jet impingement cooling in a horizontal porous layer under local thermal non-equilibrium conditions, *Int. J. Therm. Sci.* 48 (2009) 860–870.
- [24] K. Vafai, M. Sozen, Analysis of energy and momentum transport for fluid flow through a porous bed, *J. Heat Transfer*, *Trans. ASME* 112 (1994) 690–699.
- [25] A. Amiri, K. Vafai, Analysis of dispersion effects and non-thermal equilibrium, Non-Darcian, variable porosity incompressible flow through porous media, *Int. J. Heat Mass Transfer* 37 (1994) 939–959.
- [26] G.F. Al-Sumaily, H.M. Hussen, W.H. Alawee, H.A. Dahad, M.C. Thompson, Non-Darcian Bénard convection in eccentric annuli containing spherical particles, *Int. J. Heat Fluid Flow* 86 (2020) 108705.
- [27] P. Cheng, Mixed convection about a horizontal cylinder and a sphere in a fluid-saturated porous medium, *Int. J. Heat Mass Transf.* 25 (1982) 1245–1247.
- [28] I. Pop, M. Kumari, G. Nath, Free convection about cylinders of elliptic cross section embedded in a porous medium, *Int. J. Eng. Sci.* 30 (1992) 35–45.
- [29] K. Yih, Coupled heat and mass transfer by natural convection adjacent to a permeable horizontal cylinder in a saturated porous medium, *Int. Commun. Heat Mass Transfer* 26 (1999) 431–440.
- [30] M. Kumari, S. Jayanthi, Non-Darcy free convection flow over a horizontal cylinder in a saturated porous medium, *Int. Commun. Heat Mass Transfer* 31 (2004) 1219–1226.
- [31] S. Ergun, Fluid flow through packed columns, *Chem. Eng. Progress* 48 (1952) 89–94.
- [32] F.A. Dullien, *Porous Media: Fluid Transport and Pore Structure*, Academic Press, New York, 1979.
- [33] N. Wakao, S. Kaguei, T. Funazkri, Effect of fluid dispersion coefficients on particle-to-fluid heat transfer coefficients in packed beds- correlation of Nusselt numbers, *Chem. Eng. Sci.* 34 (1979) 325–336.
- [34] N. Wakao, S. Kaguei, *Heat and Mass Transfer in Packed Beds*, Gordon and Breach, New York, 1982.
- [35] P. Zehner, E.U. Schluender, Thermal conductivity of granular materials at moderate temperatures, *Chem.-Ingenieur-Tech.* 42 (1970) 933–941.
- [36] G.E. Karniadakis, M. Israeli, S.A. Orszag, High-order splitting methods for the incompressible Navier-Stokes equations, *J. Comput. Phys.* 97 (1991) 414–443.
- [37] M.C. Thompson, K. Hourigan, A. Cheung, T. Leweke, Hydrodynamics of a particle impact on a wall, *Appl. Math. Model.* 30 (2006) 1356–1369.
- [38] C.A.J. Fletcher, *Computational Galerkin Methods*, Springer-Verlag, New York, 1984.
- [39] C.A.J. Fletcher, *Computational Techniques for Fluid Dynamics*, Vol. 1, Springer-Verlag, New York, 1991.
- [40] G.E. Karniadakis, S.J. Sherwin, *Spectral/Hp Methods for Computational Fluid Dynamics*, Oxford University Press, Oxford, 2005.
- [41] A.J. Chorin, Numerical solution of the Navier-Stokes equations, *Math. Comp.* 22 (1968) 745–762.
- [42] G. Al-Sumaily, S. John, M.C. Thompson, Analysis of forced convection heat transfer from a circular cylinder embedded in a porous medium, *Int. J. Therm. Sci.* 51 (2012) 121–131.
- [43] G. Al-Sumaily, M.C. Thompson, Forced convection from a circular cylinder in pulsating flow with and without the presence of porous media, *Int. J. Heat Mass Transfer* 61 (2013) 226–244.
- [44] G. Al-Sumaily, Forced convection heat transfer from a bank of circular cylinders embedded in a porous medium, *J. Heat Transfer, ASME* 136 (2014) 042602–042602–11.
- [45] G. Al-Sumaily, M.C. Thompson, Bénard convection from a circular cylinder in a packed bed, *Int. Commun. Heat Mass Transfer* 54 (2014) 18–26.
- [46] G.F. Al-Sumaily, A. Nakayama, J. Sheridan, M.C. Thompson, The effect of porous media particle size on forced convection from a circular cylinder without assuming local thermal equilibrium between phases, *Int. J. Heat Mass Transfer* 55 (2012) 3366–3378.
- [47] G.F. Al-Sumaily, A.A. Ezzi, H.A. Dahad, M.C. Thompson, T. Yusaf, Legitimacy of the local thermal equilibrium hypothesis in porous media: A comprehensive review, *Energies* 14 (2021) 8114.
- [48] A. Abdedou, K. Bouhadef, Comparison between two local thermal non equilibrium criteria in forced convection through a porous channel, *J. Appl. Fluid Mech.* 8 (2015) 491–498.
- [49] G.F. Al-Sumaily, S. John, C.T. Mark, Validation of thermal equilibrium assumption in forced convection steady and pulsatile flows over a cylinder embedded in a porous channel, *Int. Commun. Heat Mass Transf.* 43 (2013) 30–38.
- [50] G.F. Al-Sumaily, H.M. Hussen, C.T. Mark, Validation of thermal equilibrium assumption in free convection flow over a cylinder embedded in a packed bed, *Int. Commun. Heat Mass Transf.* 58 (2014) 184–192.